

A simplified lattice Boltzmann implementation of the quasi-static approximation in pipe flows under the presence of non-uniform magnetic fields

H.S. Tavares,^{1,*} B. Magacho,¹ L. Moriconi,¹ and J. Loureiro²

¹*Instituto de Física, Universidade Federal do Rio de Janeiro,
C.P. 68528, CEP: 21945-970, Rio de Janeiro, RJ, Brazil*

²*Programa de Engenharia Mecânica,
Coordenação dos Programas de Pós-Graduação em Engenharia,
Universidade Federal do Rio de Janeiro, C.P. 68503,
CEP: 21945-970, Rio de Janeiro, RJ, Brazil*

We propose a single-step simplified lattice Boltzmann algorithm capable of performing magnetohydrodynamic (MHD) flow simulations in pipes for very small values of magnetic Reynolds numbers R_m . In some previous works, most lattice Boltzmann simulations are performed with values of R_m close to the Reynolds numbers for flows in simplified rectangular geometries. One of the reasons is the limitation of some traditional lattice Boltzmann algorithms in dealing with situations involving very small magnetic diffusion time scales associated with most industrial applications in MHD, which require the use of the so-called quasi-static (QS) approximation. Another reason is related to the significant dependence that many boundary conditions methods for lattice Boltzmann have on the relaxation time parameter. In this work, to overcome the mentioned limitations, we introduce an improved simplified algorithm for velocity and magnetic fields which is able to directly solve the equations of the QS approximation, among other systems, without preconditioning procedures. In these algorithms, the effects of solid insulating boundaries are included by using an improved explicit immersed boundary algorithm, whose accuracy is not affected by the values of R_m . Some validations with classic benchmarks and the analysis of the energy balance in examples including uniform and non-uniform magnetic fields are shown in this work. Furthermore, a progressive transition between the scenario described by the QS approximation and the MHD canonical equations in pipe flows is visualized by studying the evolution of the magnetic energy balance in examples with unsteady flows.

* hugoczpb@gmail.com.br

CONTENTS

I. Introduction	3
II. Magnetohydrodynamic equations and the quasi-static approximation	4
III. Simplified single-step lattice Boltzmann methods for MHD flows	6
A. Traditional lattice Boltzmann method	6
B. Connection with hydrodynamic equations	9
C. Single-step lattice Boltzmann algorithm for the Navier-Stokes equations	10
D. Single-step simplified LBM algorithm for the magnetic fields equations	11
E. Summary of the one-stage simplified LBM algorithm for MDH flows	13
IV. Validations and benchmarks	14
V. Improved simplified single-step LBM algorithm	16
A. Improvement in the implementation of forcing terms	16
B. Boundary condition-enforced IBM	17
C. Explicit boundary condition-enforced IBM	20
D. Explicit boundary condition-enforced IBM for magnetic field	22
E. Viscosity-independent boundary condition-enforced IBM	23
F. Resistivity-independent boundary condition-enforced IBM	26
G. Stability improvements for high values of viscosity and resistivity	27
H. Strategies for very high values of resistivity	31
VI. Effects of non-uniform magnetic fields	36
VII. Simulations with magnetic Prandtl number $Pr_m > 1$	39
VIII. Conclusions	43
Acknowledgements	44
References	44

I. INTRODUCTION

Magnetohydrodynamics (MHD) flows are found in nature and in industrial applications involving many conductive fluids and plasma flows. In most of industrial applications, for example, the magnetic Reynolds number R_m is very often smaller than 10^{-2} [1]. Simulations involving small values R_m are usually performed by using the so-called quasi-static (QS) approximation, where the induced magnetic fluctuations are considered much smaller than the applied magnetic field [1–3]. The derivation of the QS approximation involves taking the limit of vanishing R_m , which can introduce several challenges from the numerical point of view. One of the biggest difficulties is associated with the need of solutions for a separate evolution equation for the magnetic field, and another difficulty comes with the presence of a very small diffusion time scale. Due to these difficulties, many numerical works in MHD have been restricted to cases where the magnetic Prandtl number Pr_m is close to 1, i.e., where the magnetic and kinetic time scales are the same. This is also the case in many numerical works in the literature of the lattice Boltzmann methods (LBM) [4–7]. In [5, 7], simulations with very small Pr_m are performed but only in the context of stationary flows.

One of the main objectives in this article is to approach the equations of the QS regime by only using a lattice Boltzmann framework. More specifically, we aim to extend the simplified lattice Boltzmann models proposed in [4, 8] for simulations of MHD flows involving curved boundaries with very small values of magnetic Reynolds numbers. In this analysis, we also intend to study the transition between the regime described by the canonical MHD equations and the regime characteristic of the QS approximation [2]. In our study, we manage to analyse not only the transition, but also regimes with $R_m \ll 1$, characteristic of industrial applications.

In the original simplified single-step LBM [8], the straightforward introduction of the forcing terms does not take into consideration the lattice discrete effects, as pointed by [9, 10] in some analogous simplified LBM models. Also, many simplified models have limitations with respect to the stability and accuracy for high values of relaxation times, the same limitation also appears in the classical LBM-BGK model [11, 12], which can be seen as one of the main limitations of this model towards simulations with small values of R_m . Another issue is associated with the dependence on the relaxation time parameter that some boundary conditions methods for LBM have, as pointed out by [13]. The influence of curved boundaries was not addressed by [4] in the context of MHD flows, and in the Ref. [5], the only simulation involving curved boundaries is performed with $Pr_m = 1$.

By considering the recent advances provided by the works [9, 13, 14], we manage to overcome many of the limitations of the previous lattice Boltzmann models by introducing an improved simplified LBM framework able to perform simulations of the QS approximation in flows with curved insulating boundaries up to $Pr_m \sim 10^{-7}$ in the laminar regime. Not only that, by considering preconditioning procedures [5, 7, 15–17], we also manage to perform some simulations with $Pr_m > 1$, a regime characterized by fast fluctuations of the magnetic fields, which require the use of more accurate numerical methods. In the LBM literature, to the best of our knowledge, only a few studies [18, 19] analyzed MHD flows in this regime, showing accurate results up to $Pr_m = 2$.

This article is organized as follows. In the first part, Section II, we describe the general MHD equations and its connections with the quasi-static approximations, enumerating some important differences between the two systems from the numerical point of view. In Section III, we briefly introduce the traditional lattice Boltzmann method. In the following, we discuss a recent simplified single-step LBM algorithm for MHD flows based on the research developed by [4, 8]. In the Section IV, we describe the general structure of the verification of benchmarks and validations considered throughout the article. In Section V, the single-step algorithm undergoes to a series of improvements, where increase of stability and accuracy are proposed with a some numerical validations. In the same section, a viscosity- and resistivity-independent immersed boundary method (IBM) able to simulate flows in the quasi-static regime is proposed. In Section VI, we apply the improvements developed in the previous sections for MHD flows involving non-uniform magnetic fields. In Section VII, techniques for the simulation of regimes with $Pr_m > 1$ are developed with some numerical validations; and in Section VIII, we provide some conclusions and perspectives.

II. MAGNETOHYDRODYNAMIC EQUATIONS AND THE QUASI-STATIC APPROXIMATION

The equations describing magnetohydrodynamic phenomena are formed by a coupling between the continuity and the Navier–Stokes equations for describing the fluid motion, and the Maxwell’s equations for electromagnetism as follows [1]

$$\rho \left(\frac{\partial \mathbf{u}}{\partial t} + (\mathbf{u} \cdot \nabla) \mathbf{u} \right) = -\nabla p + \mu \nabla^2 \mathbf{u} + \mathbf{J} \times \mathbf{B}, \quad (1)$$

$$\nabla \cdot \mathbf{u} = 0, \quad (2)$$

$$\frac{\partial \mathbf{B}}{\partial t} + \nabla \cdot (\mathbf{u} \otimes \mathbf{B} - \mathbf{B} \otimes \mathbf{u}) = \eta \nabla^2 \mathbf{B}, \quad (3)$$

$$\nabla \cdot \mathbf{B} = 0, \quad (4)$$

where \mathbf{u} and \mathbf{B} are the velocity and magnetic fields respectively, η is the magnetic resistivity and μ is the dynamic viscosity of the fluid. We denote by $\nu = \mu/\rho$ the kinematic viscosity. For the sake of simplicity, in the rest of the article, we denote $\mathbf{u} \otimes \mathbf{B} = \mathbf{u}\mathbf{B}$ and $\mathbf{B} \otimes \mathbf{u} = \mathbf{B}\mathbf{u}$. The electric field \mathbf{E} and the electric current density \mathbf{J} are approximated by

$$\mathbf{E} = -(\mathbf{u} \times \mathbf{B}) + \eta(\nabla \times \mathbf{B}), \quad \mathbf{J} = \nabla \times \mathbf{B}. \quad (5)$$

Considering a system where U_0 is the characteristic velocity, B_0 is the characteristic magnetic intensity and L is the typical length scale. We have the following important dimensionless quantities

$$\text{Re} = \frac{U_0 L}{\nu}, \quad R_m = \frac{U_0 L}{\eta}, \quad \text{Ha} = \frac{B_0 L}{\sqrt{\eta \nu}}, \quad \text{Pr}_m = \frac{\eta}{\nu}, \quad (6)$$

which are respectively: the Reynolds number, the magnetic Reynolds number, the Hartman number and the magnetic Prandtl number. In our study, we are mainly interested in the situations where $R_m \ll 1$, characteristic of the QS approximation [1], in pipe flows as shown schematically in Figure 1. In this regime is convenient to introduce the decomposition $\mathbf{B} = \mathbf{B}^{ext} + \delta\mathbf{B}$, where \mathbf{B}^{ext} is the external imposed magnetic field and $\delta\mathbf{B}$ are fluctuations. The QS approximation translates into assuming $\|\delta\mathbf{B}\| \ll \|\mathbf{B}^{ext}\|$.

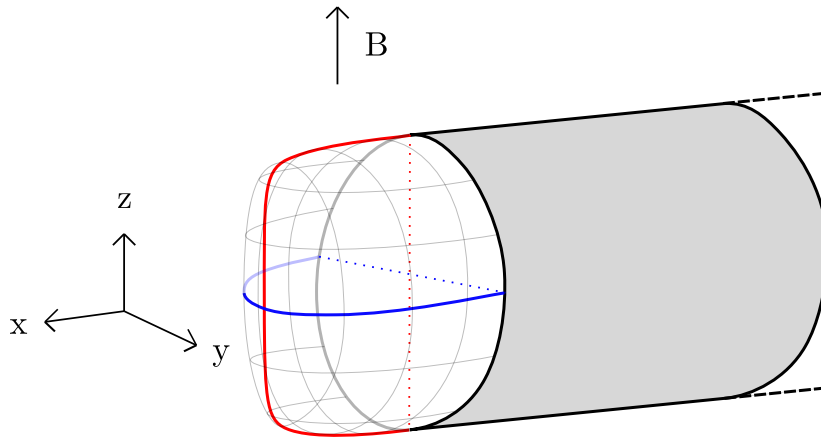


FIG. 1. Schematic representation of MHD pipe flow with a transversal magnetic field. The red and blue lines correspond to some important cross sections of the velocity field that are analyzed in detail in this article. The analysis of these sections helps clarify what are the main effects of constant transverse magnetic fields.

The following system holds in this regime [2]

$$\rho \left(\frac{\partial \mathbf{u}}{\partial t} + (\mathbf{u} \cdot \nabla) \mathbf{u} \right) = -\nabla p + \mu \nabla^2 \mathbf{u} + \mathbf{J} \times \mathbf{B}, \quad (7)$$

$$\nabla \cdot \mathbf{u} = 0, \quad (8)$$

$$\eta \nabla^2 \mathbf{B} = \nabla \cdot (\mathbf{u} \mathbf{B}^{ext} - \mathbf{B}^{ext} \mathbf{u}), \quad (9)$$

$$\nabla \cdot \mathbf{B} = 0. \quad (10)$$

This approximation does not involve the problems with very small magnetic diffusion time scales. The convection-diffusion equation (3) for a magnetic field is replaced by a Poisson equation (9). A first difficulty comes with these changes, which is the fact that usually the lattice Boltzmann methods are not constructed to solve such types of equations. Also, in many problems, the solutions of Poisson equations involve non-local methods, which can be a problem if the objective is to perform parallelized simulations.

In the next sections, we aim to approach the system (7-10) by using a lattice Boltzmann framework. In this approach, the problems with the very different diffusive time scales are handled by considering the asymptotic properties of a simplified LBM solver for advection-diffusion equations in order to treat the Poisson equation (9). The influence of curved walls is included by using an explicit immersed boundary method whose accuracy is not significantly affected by the coefficients of viscosity and resistivity. We also discuss lattice Boltzmann implementations of system (1-4) for some simulations of pipe flows with $Pr_m > 1$. In the following sections, a detailed description of the described methods will be shown.

III. SIMPLIFIED SINGLE-STEP LATTICE BOLTZMANN METHODS FOR MHD FLOWS

A. Traditional lattice Boltzmann method

The starting point of the lattice Boltzmann method is the connection between the Boltzmann equation and the classical hydrodynamics equations. The Boltzmann equation is an integro-differential equation for the probability density function $f(\mathbf{x}, \mathbf{v}, t)$ in six-dimensional space of a particle position $\mathbf{x} \in \mathbb{R}^3$ and momentum $\mathbf{v} \in \mathbb{R}^3$ given by

$$\partial_t f + \nabla_{\mathbf{x}} f \cdot \mathbf{v} + \frac{\mathbf{F}_{ext}}{\rho} \cdot \nabla_{\mathbf{v}} f = Q(f, f), \quad (11)$$

where $Q(f, f)$ is collision integral, \mathbf{F}_{ext} is the body force, ρ is macroscopic mass density of the system, and $\nabla_{\mathbf{x}}$ and $\nabla_{\mathbf{v}}$ are gradients with respect to the position \mathbf{x} and velocity \mathbf{v} coordinates, respectively.

It can be shown that the collision integral $Q(f, f)$ has at least five invariants [20], i.e., a set of functions ξ_k , $k = 1, 2, 3, 4, 5$, satisfying

$$\int_{\mathbb{R}^3} \xi_k(\mathbf{v}) Q(f, f) d\mathbf{v} = 0, \quad (12)$$

which are $\xi_1 = 1$, $(\xi_2, \xi_3, \xi_4) = \mathbf{v}$ and $\xi_5 = |\mathbf{v}|^2$. A general collision invariant can be written as linear combinations of the functions ξ_k . The invariants are associated to some important macroscopic quantities in the system, some of them are

$$\text{mass density: } \int f d\mathbf{v} = \rho, \quad (13)$$

$$\text{momentum: } \int f \mathbf{v} d\mathbf{v} = \rho \mathbf{u}. \quad (14)$$

A set of conservation laws for each of these quantities can be obtained multiplying the Boltzmann equation (11) by a collision invariant and subsequently integrating with respect to the velocity.

In the lattice Boltzmann method (LBM) the basic quantity is the discrete-velocity distribution function $f_i(\mathbf{x}, t)$, it represents the density of particles with velocity \mathbf{c}_i at position \mathbf{x} and time t . By discretizing the Boltzmann equation (11) in velocity space, physical space, and time, we obtain the discrete Boltzmann equation [11, 12]

$$f_i(\mathbf{x} + \mathbf{c}_i \Delta t, t + \Delta t) = f_i(\mathbf{x}, t) + \Omega_i(\mathbf{x}, t), \quad (15)$$

where $\Omega_i(\mathbf{x}, t)$ is the discrete version of the collision integral in (11). This equation expresses that a particle $f_i(\mathbf{x}, t)$ moves with velocity \mathbf{c}_i to the nearest neighbors after a time step δt , i.e., the grid spacing is giving by $\delta x = |\mathbf{c}_i| \delta t$. Analogously, the mass density and momentum density $\rho \mathbf{u}$ at (\mathbf{x}, t) can be found through weighted sums known as moments of f_i as

$$\rho(\mathbf{x}, t) = \sum_i f_i(\mathbf{x}, t), \quad (16)$$

$$\rho(\mathbf{x}, t) \mathbf{u}(\mathbf{x}, t) = \sum_i \mathbf{c}_i f_i(\mathbf{x}, t), \quad (17)$$

in a similar fashion to (13) and (14). The main difference between f_i and the continuous distribution function f is that all of the argument variables of f_i are discrete, with the subscript i referring to a finite discrete set of velocities \mathbf{c}_i as shown in Figure 2.

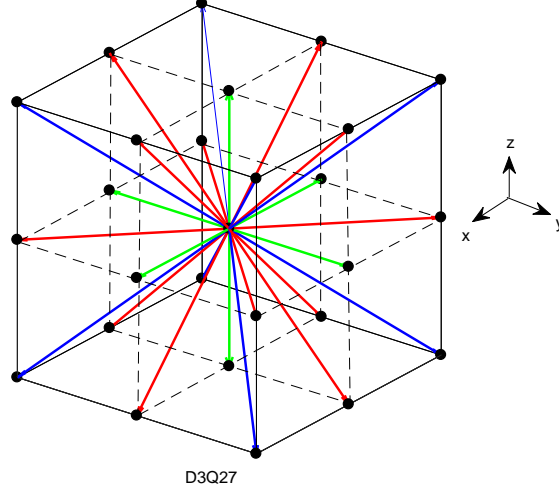


FIG. 2. Lattice velocities for D3Q27 scheme.

The discrete collision integral Ω_i is given by BGK operator defined as

$$\Omega_i(f, f) = -\frac{f_i - f_i^{(eq)}}{\tau}, \quad (18)$$

where the equilibrium distribution is given by

$$f_i^{(eq)}(\rho, \mathbf{u}) = w_i \rho \left(1 + \frac{\mathbf{c}_i \cdot \mathbf{u}}{c_s^2} + \frac{(\mathbf{c}_i \cdot \mathbf{u})^2}{2c_s^4} - \frac{\mathbf{u} \cdot \mathbf{u}}{2c_s^2} \right), \quad (19)$$

where c_s is the speed of sound given by $c_s = c/\sqrt{3}$ and w_i are the lattice weights associated with the velocity scheme D3Q27 as shown in Table I.

Velocities \mathbf{c}_i	Number	Weight w_i
(0,0,0)	1	8/27
($\pm 1, 0, 0$), ($0, \pm 1, 0$), ($0, 0, \pm 1$)	6	2/27
($\pm 1, \pm 1, 0$), ($\pm 1, 0, \pm 1$), ($0, \pm 1, \pm 1$)	12	1/54
($\pm 1, \pm 1, \pm 1$)	8	1/216

TABLE I. Weights for the velocity scheme D3Q27.

Using the BGK approximation in the equation (15), we obtain the lattice BGK equation

$$f_i(\mathbf{x} + \mathbf{c}_i \delta t, t + \delta t) = f_i(\mathbf{x}, t) - \frac{1}{\tau} \left(f_i(\mathbf{x}, t) - f_i^{(eq)}(\rho, \mathbf{u}) \right). \quad (20)$$

The simplest way to initialize the populations at the initial time $t = 0$ is to set $f_i(\mathbf{x}, t = 0) = f_i^{(eq)}(\rho(\mathbf{x}, t = 0), \mathbf{u}(\mathbf{x}, t = 0))$. The kinematic viscosity ν is connected to the relaxation time τ by the equation

$$\nu = c_s^2 \left(\tau - \frac{1}{2} \right) \delta t. \quad (21)$$

The BGK scheme is the most traditional LBM algorithm with many interesting applications, but it has well known limitations in terms of stability, memory requirements and some problems with appropriate boundary conditions methods for some types of complex multiphysics simulations [11, 12].

In the next section, we discuss a recent approach that began with works developed by [8, 21, 22], later extended to MHD flows by [4], towards a simplified lattice Boltzmann method that does not involve the evolution of the non-equilibrium distributions. In this approach, a single-step algorithm is formulated giving a more efficient method in terms of memory requirements and stability in comparison with the traditional BKG algorithm (20), while keeping almost the same accuracy.

B. Connection with hydrodynamic equations

From (15), we can derive solutions for Navier-Stokes by first considering a 2nd-order Taylor series expansion in time and space given by

$$f_i(\mathbf{x} + \mathbf{c}_i \delta t, t + \delta t) - f_i(\mathbf{x}, t) = \delta t D_i f_i + \frac{\delta t^2}{2} D_i^2 f_i + O(\delta t^2), \quad (22)$$

where $D_i = \frac{\partial}{\partial t} + \mathbf{c}_i \cdot \nabla$ denotes the material derivative. Up to a second order error, we have [23]

$$\frac{\partial}{\partial t} f_i + \mathbf{c}_i \cdot \nabla f_i + \delta t \left(\frac{1}{2} \mathbf{c}_1 \otimes \mathbf{c}_1 : \nabla \nabla f_i + \mathbf{c}_i \cdot \nabla \frac{\partial f_i}{\partial t} + \frac{1}{2} \frac{\partial^2 f_i}{\partial t^2} \right) = -\frac{1}{\tau \delta t} (f_i - f_i^{eq}). \quad (23)$$

Next, consider the Chapman-Enskog multiscale expansion [24],

$$\frac{\partial}{\partial t} = \varepsilon \frac{\partial}{\partial t_1} + \varepsilon^2 \frac{\partial}{\partial t_2}, \quad \nabla = \varepsilon \nabla_1. \quad (24)$$

where ε is a small parameter proportional to the Knudsen number [12]. In this expansion, it is assumed that the diffusion time scale t_2 is much larger than the convective time scale t_1 , and that diffusion and convection act on the same spatial scale [20]. In similar fashion, the distribution function f_i can be expanded about the local equilibrium distribution function f_i^{eq} as

$$f_i = f_i^{eq} + \varepsilon f_i^{neq}, \quad (25)$$

where $f_i^{neq} = f_i^{(1)} + \varepsilon f_i^{(2)} + O(\varepsilon^2)$ is the nonequilibrium distribution, which is associated with viscous dissipation and verifies the following constraints

$$\sum_i f_i^{(k)} = 0, \quad \sum_i f_i^{(k)} \mathbf{c}_i = 1, \quad \text{for } k = 1, 2, \quad (26)$$

called solvability conditions. Substituting (24) and (25) into (23) and combining the sequence of equations obtained up to order $O(\varepsilon^2)$, we obtain the following system [11, 12]

$$\sum_{i=0}^N \left[\frac{\partial f_i^{eq}}{\partial t} + \mathbf{c}_i \cdot \nabla f_i^{eq} \right] = 0, \quad (27)$$

$$\sum_{i=1}^N \mathbf{c}_i \left[\frac{\partial f_i^{eq}}{\partial t} + \mathbf{c}_i \cdot \nabla f_i^{eq} + \left(1 - \frac{1}{2\tau} \right) D_i f_i^{(1)} \right] = 0, \quad (28)$$

with

$$f_i^{(1)}(\mathbf{x}, t) \simeq -\tau \delta t D_i f_i^{eq}(\mathbf{x}, t) = -\tau \delta t \left(\frac{\partial}{\partial t} + \mathbf{c}_i \cdot \nabla \right) f_i^{eq}(\mathbf{x}, t). \quad (29)$$

By using the moments (16), (17) and (26), it follows that the equations (27) and (28) can be turned into solutions for continuity and Navier-Stokes equations respectively [11].

C. Single-step lattice Boltzmann algorithm for the Navier-Stokes equations

The equations (27) and (28) are the starting point of many simplified LBM algorithms [8, 21, 22]. Different discretization schemes for these equations produce different simplified algorithms. In this article, the starting point is the approach developed by [8], which will be described in the following with a slightly different derivation.

Considering the finite differences

$$\frac{\partial f_\alpha^{eq}}{\partial t} = \frac{f_\alpha^{eq}(\mathbf{x}, t + \delta t) - f_\alpha^{eq}(\mathbf{x}, t)}{\delta t}, \quad (30)$$

$$\mathbf{c}_\alpha \cdot \nabla f_\alpha^{eq} = -\frac{f_i^{eq}(\mathbf{x} + \mathbf{c}_i \delta t, t) - 4f_i^{eq}(\mathbf{x}, t) + 3f_i^{eq}(\mathbf{x} - \mathbf{c}_i \delta t, t)}{2\delta x}, \quad (31)$$

we can rewrite (27) as

$$\sum_{i=1}^N \frac{f_i^{eq}(\mathbf{x}, t + \delta t) - f_i^{eq}(\mathbf{x}, t)}{\delta t} - \frac{f_i^{eq}(\mathbf{x} + \mathbf{c}_i \delta t, t) - 4f_i^{eq}(\mathbf{x}, t) + 3f_i^{eq}(\mathbf{x} - \mathbf{c}_i \delta t, t)}{2\delta x} = 0. \quad (32)$$

Using (16), we arrive in the following algorithm

$$\rho(\mathbf{x}, t + \delta t) = \frac{3}{2} \sum_{i=1}^N f_i^{eq}(\mathbf{x} - \mathbf{c}_i \delta t, t) - \sum_{i=1}^N f_i^{eq}(\mathbf{x}, t) + \frac{1}{2} \sum_{i=1}^N f_i^{eq}(\mathbf{x} + \mathbf{c}_i \delta t, t). \quad (33)$$

For the momentum equation (28), the term $\mathbf{c}_i \cdot \nabla f_i^{eq}$ is discretized in a different way as

$$\mathbf{c}_i \cdot \nabla f_i^{eq} = \frac{f_i^{eq}(\mathbf{x} + \mathbf{c}_i \delta t, t) - f_i^{eq}(\mathbf{x} - \mathbf{c}_i \delta t, t)}{2\delta x}. \quad (34)$$

For the non-equilibrium term (29), we apply the directional approach for the gradient operation

$$\sum_{i=1}^N \mathbf{c}_i D_i f_i^{(1)} = \sum_{i=1}^N \mathbf{c}_i (\mathbf{c}_i \cdot \nabla f_i^{(1)}) = \sum_{i=1}^N \mathbf{c}_i \frac{\partial f_i^{(1)}}{\partial \mathbf{c}_i}, \quad (35)$$

where we used the constraints in (26). Using (29), we have

$$\begin{aligned} \sum_{i=1}^N \mathbf{c}_i \frac{\partial f_i^{(1)}}{\partial \mathbf{c}_i} &\simeq \sum_{i=1}^N \mathbf{c}_i \frac{\partial}{\partial \mathbf{c}_i} \left(-\tau \delta t \frac{\partial f_i^{eq}}{\partial \mathbf{c}_i} \right), \\ &\simeq \sum_{i=1}^N -\tau \delta t \mathbf{c}_i \frac{\partial}{\partial \mathbf{c}_i} \left(\frac{f_i^{eq}(\mathbf{x} + \mathbf{c}_i \delta t, t) - f_i^{eq}(\mathbf{x}, t)}{\delta x} \right), \\ &\simeq \sum_{i=1}^N -\tau \delta t \mathbf{c}_i \left(\frac{f_i^{eq}(\mathbf{x} + \mathbf{c}_i \delta t, t) - 2f_i^{eq}(\mathbf{x}, t) + f_i^{eq}(\mathbf{x} - \mathbf{c}_i \delta t, t)}{(\delta x)^2} \right), \end{aligned} \quad (36)$$

where we combined forwards and backwards finite differences for the operator $\frac{\partial}{\partial \mathbf{c}_i}$.

Substituting (32), (34) and (36) into (28), and considering (17) it follows that

$$\begin{aligned} \rho(\mathbf{x}, t + \delta t) \mathbf{u}(\mathbf{x}, t + \delta t) &= \sum_{i=1}^N \{ \mathbf{c}_i f_i^{eq}(\mathbf{x} - \mathbf{c}_i \delta t, t) + \\ &\quad + (\tau - 1) \mathbf{c}_i [f_i^{eq}(\mathbf{x} + \mathbf{c}_i \delta t, t) - 2f_i^{eq}(\mathbf{x}, t) + f_i^{eq}(\mathbf{x} - \mathbf{c}_i \delta t, t)] \}. \end{aligned} \quad (37)$$

The equations (33) and (37) constitute the single-step lattice Boltzmann algorithm [8]. It is important to observe that these formulas depend only on the equilibrium distributions, which are only associated with the macroscopic quantities of the system. This feature reduces significantly the memory requirements in comparison to the traditional BGK algorithm, and also simplifies the implementation of boundary conditions, as we no longer have to deal with complicated manipulations of non-equilibrium distributions at the boundaries. In the next section, we consider a similar development in the context of the advection-diffusion equation (3) for the canonical MHD system.

D. Single-step simplified LBM algorithm for the magnetic fields equations

In [25], Dellar derived an extension of the lattice BKG scheme (20) that solves the advection-diffusion equation (3) for the magnetic field. This work also presents, in a similar fashion, the following algorithm

$$g_{ix}(\mathbf{x} + \mathbf{c}_i \delta t, t + \delta t) = g_{ix}(\mathbf{x}, t) - \frac{1}{\tau_m} (g_{ix}(\mathbf{x}, t) - g_{ix}^{eq}(\mathbf{x}, t)), \quad (38)$$

which solves, for example, the x-components of the magnetic field as

$$B_x(\mathbf{x}, t) = \sum_{i=1}^N g_{ix}(\mathbf{x}, t). \quad (39)$$

The relationship between resistivity η and the relaxation parameter τ_m is given by

$$\eta = c_s^2 \left(\tau_m - \frac{1}{2} \right), \quad (40)$$

where c_s is the corresponding speed of sound. An analogous equilibrium distribution is defined as

$$g_{ix}^{eq}(\mathbf{x}, t) = w_i \left[B_x + \frac{c_{iy}}{c_s^2} (u_y B_x - u_x B_y) + \frac{c_{iz}}{c_s^2} (u_z B_x - u_x B_z) \right]. \quad (41)$$

In the work [4], the authors introduced a single-step (or one-stage) simplified LBM algorithm for (3) following the same steps of [8], as we describe as follows.

The lattice Boltzmann equation (LBE) can be written as

$$g_{ix}(\mathbf{x} + \mathbf{c}_i \delta t) - g_i(\mathbf{x}, t) = \frac{g_{ix}^{eq}(\mathbf{x}, t) - g_{ix}(\mathbf{x}, t)}{\tau_m}. \quad (42)$$

By applying a Taylor series expansion at the left-hand side of (42) followed by a Chapman–Enskog expansion up to second order, it is possible to write the following equation

$$\sum_i \left[\frac{\partial g_{ix}^{eq}}{\partial t} + \mathbf{c}_i \cdot \nabla g_{ix}^{eq} + \left(1 - \frac{1}{2\tau_m} \right) D_i g_{ix}^{(1)} \right] = 0, \quad (43)$$

with

$$g^{(1)}(\mathbf{x}, t) \simeq -\tau_m \delta t D_i g_i^{eq} = -\tau_m \delta t \left(\frac{\partial}{\partial t} + \mathbf{c}_i \cdot \nabla \right) g_i^{eq}(\mathbf{x}, t). \quad (44)$$

Now consider the following finite differences schemes

$$\frac{\partial g_{ix}^{(0)}}{\partial t} = \frac{g_{ix}^{(0)}(\mathbf{x} + \mathbf{c}_i \Delta t, t) - g_{ix}^{(0)}(\mathbf{x}, t)}{\delta t}, \quad (45)$$

$$\mathbf{c}_i \cdot \nabla g_{ix}^{(0)} = \frac{g_{ix}^{(0)}(\mathbf{x} + \mathbf{c}_i \delta t, t) - g_{ix}^{(0)}(\mathbf{x} - \mathbf{c}_i \delta t, t)}{2\delta x}, \quad (46)$$

and

$$\begin{aligned} \sum_{i=1}^N \mathbf{c}_i D_i g_{ix}^{(1)} &= \sum_{i=1}^N \mathbf{c}_i (\mathbf{c}_i \cdot \nabla g_{ix}^{(1)}) \simeq \sum_{i=1}^N \mathbf{c}_i \frac{g_{ix}^{(1)}(\mathbf{x} + \mathbf{c}_i \delta t, t) - g_{ix}^{(1)}(\mathbf{x}, t)}{\delta x} \simeq \\ &\simeq \sum_{i=1}^N -\mathbf{c}_i \tau_m \delta t \frac{[g_{ix}^{eq}(\mathbf{x} + \mathbf{c}_i \delta t, t) - 2g_{ix}^{eq}(\mathbf{x}, t) + g_{ix}^{eq}(\mathbf{x} - \mathbf{c}_i \delta t, t)]}{(\delta x)^2}. \end{aligned} \quad (47)$$

So it follows that

$$\begin{aligned} &\sum_i [g_{ix}^{eq}(\mathbf{x}, t + \delta t) + 2(\tau_m - 1)g_{ix}^{eq}(\mathbf{x}, t) - \\ &-(\tau_m - 1)g_{ix}^{eq}(\mathbf{x} + \mathbf{c}_i \delta t, t) - \tau_m g_{ix}^{eq}(\mathbf{x} - \mathbf{c}_i \delta t, t)] = 0, \end{aligned} \quad (48)$$

and then,

$$B_x(\mathbf{x}, t + \delta t) = \sum_{i=1}^N \{g_{ix}^{eq}(\mathbf{x} - \mathbf{c}_i \delta t, t) + (\tau_m - 1)[g_{ix}^{eq}(\mathbf{x} + \mathbf{c}_i \delta t, t) - 2g_{ix}^{eq}(\mathbf{x}, t) + g_{ix}^{eq}(\mathbf{x} - \mathbf{c}_i \delta t, t)]\}. \quad (49)$$

Analogously, the algorithm is only a function of the equilibrium distribution given by (41). This algorithm is also usually much more stable than the traditional form (38).

E. Summary of the one-stage simplified LBM algorithm for MDH flows

Considering the following expressions for the equilibrium distributions:

$$f_i^{eq}(\mathbf{x}, t) = w_i \rho \left(1 + \frac{\mathbf{c}_i \cdot \mathbf{u}}{c_s^2} + \frac{(\mathbf{c}_i \cdot \mathbf{u})^2}{2c_s^4} - \frac{\mathbf{u} \cdot \mathbf{u}}{2c_s^2} \right), \quad (50)$$

$$g_{ix}^{eq}(\mathbf{x}, t) = w_i \left[B_x + \frac{c_{iy}}{c_s^2} (u_y B_x - u_x B_y) + \frac{c_{iz}}{c_s^2} (u_z B_x - u_x B_z) \right], \quad (51)$$

$$g_{iy}^{eq}(\mathbf{x}, t) = w_i \left[B_y + \frac{c_{ix}}{c_s^2} (u_x B_y - u_y B_x) + \frac{c_{iz}}{c_s^2} (u_z B_y - u_y B_z) \right], \quad (52)$$

$$g_{iz}^{eq}(\mathbf{x}, t) = w_i \left[B_z + \frac{c_{ix}}{c_s^2} (u_x B_z - u_z B_x) + \frac{c_{iy}}{c_s^2} (u_y B_z - u_z B_y) \right]. \quad (53)$$

We have the following single-step (or one-stage) LBM algorithm for MHD flows

$$\begin{aligned} \rho(\mathbf{x}, t + \delta t) &= \sum_{i=1}^N \frac{3}{2} f_i^{eq}(\mathbf{x} - \mathbf{c}_i \delta t, t) - f_i^{eq}(\mathbf{x}, t) + \frac{1}{2} f_i^{eq}(\mathbf{x} + \mathbf{c}_i \delta t, t), \\ \rho(\mathbf{x}, t + \delta t) \mathbf{u}(\mathbf{x}, t + \delta t) &= \sum_{i=1}^N \mathbf{c}_i \{f_i^{eq}(\mathbf{x} - \mathbf{c}_i \delta t, t) + \\ &\quad + (\tau - 1)[f_i^{eq}(\mathbf{x} + \mathbf{c}_i \delta t, t) - 2f_i^{eq}(\mathbf{x}, t) + f_i^{eq}(\mathbf{x} - \mathbf{c}_i \delta t, t)]\}, \\ \mathbf{B}(\mathbf{x}, t + \Delta t) &= \sum_{i=1}^N \{\mathbf{g}_i^{eq}(\mathbf{x} - \mathbf{c}_i \delta t, t) + \\ &\quad + (\tau_m - 1)[\mathbf{g}_i^{eq}(\mathbf{x} + \mathbf{c}_i \delta t, t) - 2\mathbf{g}_i^{eq}(\mathbf{x}, t) + \mathbf{g}_i^{eq}(\mathbf{x} - \mathbf{c}_i \delta t, t)]\}, \end{aligned} \quad (54)$$

where $\mathbf{B} = [B_x, B_y, B_z]$ and $\mathbf{g}_i^{eq} = [g_{ix}^{eq}, g_{iy}^{eq}, g_{iz}^{eq}]$. External forcing terms \mathbf{F}_{ext} are usually added in a straightforward way as

$$\begin{aligned} \rho(\mathbf{x}, t + \delta t) \mathbf{u}(\mathbf{x}, t + \delta t) &= \sum_{i=1}^N \mathbf{c}_i \{f_i^{eq}(\mathbf{x} - \mathbf{c}_i \delta t, t) + \\ &\quad + (\tau - 1)[f_i^{eq}(\mathbf{x} + \mathbf{c}_i \delta t, t) - 2f_i^{eq}(\mathbf{x}, t) + f_i^{eq}(\mathbf{x} - \mathbf{c}_i \delta t, t)]\} + \\ &\quad + \mathbf{F}_{ext} \delta t. \end{aligned} \quad (55)$$

Dirichlet boundary conditions for geometries formed by flat boundaries are implemented straightforward by just assigning the desired values to the boundary points, some other types of boundary conditions are also implemented very similarly to conventional MHD solvers. To the best of our knowledge, no studies of the single-step LBM algorithm have been conducted in the context of MHD flows involving curved boundaries. The success of the use of the immersed boundary methods [11] in some previous lattice Boltzmann models [13, 21, 26] indicates an interesting direction for the inclusion of curved boundaries in simulations of MHD flows.

It is important to observe that the inclusion of the forcing terms by using (55) does not consider the so-called lattice discrete effects [9], associated to the correct consideration of contribution of the forcing term $\frac{\mathbf{F}_{ext}}{\rho} \cdot \nabla_{\mathbf{v}} f$ in the equation (11). This limitation can compromise the accuracy of the simulations, especially in the cases involving non-uniform or unsteady forcing terms.

Another limitation of the algorithm (54) is associated with the loss of stability and accuracy for high values of relaxation times. Considering $\delta t = \delta x = 1$, the simulations become easily unstable for values of relaxation times $\tau > 0.5$ and $\tau_m > 0.5$, a similar limitation is also shared by other simplified methods. In our work, one of the main objectives is to solve the quasi-static approximation in MHD, and for this objective it is necessary to consider high values of resistivity η which usually implies in very high values of τ_m .

In the next sections, we address all of the mentioned limitations. We first consider an implementation of forcing scheme that takes into consideration the effects of variable forcing terms in a more accurate way. Next, we consider extensions of the simplified LBM algorithms for regimes of high values of relaxation times. In the final part, we introduce explicit immersed boundary algorithms for simulations of flows involving curved boundaries and whose accuracy is independent of the values of resistivity and viscosity coefficients.

IV. VALIDATIONS AND BENCHMARKS

In the next sections, we introduce some improvements in the simplified single-step algorithm (54) and we show a series of numerical tests and validations for periodic flows in circular pipes with insulating boundaries in order to verify the suggested improvements. The numerical tests are described in more details as follows.

For examples involving stationary flows under the presence of a uniform magnetic field with insulating walls, as represented in Figure 1, we compare the numerical solutions with the analytical solution derived by Richard R. Gold [27] for a pipe flow submitted to a constant transverse magnetic

field. The Gold's solutions for the streamwise components of velocity and magnetic fields of the system (1-4) are given by

$$U_x(r, \theta) = -\frac{R^2}{\nu Ha} \frac{\partial p}{\partial x} \left[\cosh(\alpha r \cos \theta) \sum_{n=0}^{\infty} \epsilon_n \frac{I'_{2n}(\alpha)}{I_{2n}(\alpha)} I_{2n}(\alpha r) \cos(2n\theta) - \sinh(\alpha r \cos \theta) \sum_{n=0}^{\infty} 2 \frac{I'_{2n+1}(\alpha)}{I_{2n+1}(\alpha)} I_{2n+1}(\alpha r) \cos((2n+1)\theta) \right], \quad (56)$$

$$B_x(r, \theta) = -\frac{1}{\sqrt{\eta\nu}} \frac{R^2}{2Ha} \frac{\partial p}{\partial x} \left[\sum_{n=-\infty}^{\infty} (\exp(-\alpha r \cos \theta) - (-1)^n \exp(\alpha r \cos \theta)) \frac{I'_n(\alpha)}{I_n(\alpha)} I_n(\alpha r) \exp(in\theta) - 2r \cos \theta \right], \quad (57)$$

where $\alpha = Ha/2$, ϵ_n equal 1 for $n = 0$ and 2 for $n > 0$. I_n is the modified Bessel function of the first kind of order n and I'_n is the respective derivative. The Hartman number, in the context of the experiments of this article, is defined as $Ha = B_0 R / \sqrt{\eta\nu}$, where B_0 is the characteristic magnetic field intensity and R is the pipe radius.

We also study the effects of non-stationary and transients flows by analysing the evolution of magnetic energy $E_m = \langle \frac{1}{2} |\mathbf{B}|^2 \rangle$ and the kinetic energy $E_k = \langle \frac{1}{2} \rho |\mathbf{u}|^2 \rangle$ (per unit of volume), where $\langle \cdot \rangle$ denotes spatial averages within a cylinder with radius smaller than the radius of the pipe. The respective variations are given by [1]

$$\begin{aligned} \frac{dE_m}{dt} &= \eta \langle \mathbf{B} \cdot \nabla^2 \mathbf{B} \rangle - \langle \mathbf{B} \cdot (\nabla \cdot (\mathbf{uB} - \mathbf{Bu})) \rangle, \\ \frac{dE_k}{dt} &= -\langle \mathbf{u} \cdot \nabla p \rangle + \mu \langle \mathbf{u} \cdot \nabla^2 \mathbf{u} \rangle + \langle \mathbf{u} \cdot (\mathbf{J} \times \mathbf{B}) \rangle. \end{aligned} \quad (58)$$

The energy budget in (58) is analysed for constant and variable forcing term. For the study of unsteady forcing terms, we analyse the effects of a variable pressure difference defined as follows

$$\frac{\partial p}{\partial x} = F_0 \cos\left(\frac{2\pi t}{T}\right), \quad (59)$$

where F_0 is a reference force intensity and T is the period.

In order to be able to verify the Gold's solutions, we first need to introduce a set of improvements in the previous single-step algorithm given by (54) and (55). In the final part of the article, we also apply the suggested algorithms for examples involving non-uniform magnetic fields. All the numerical experiments will consider the so-called lattice Boltzmann units (lbu), a simple artificial set of units with grid spacing and time step verifying $\delta t = \delta x = 1$.

V. IMPROVED SIMPLIFIED SINGLE-STEP LBM ALGORITHM

A. Improvement in the implementation of forcing terms

For the proper consideration of the forcing terms in (11) in the simplified single-step algorithm (55), we consider the introduction of a consistent forcing scheme that takes into consideration the discrete effects at the level of distribution functions, similar to the developments in [9, 10]. In this section, we include the GZS forcing scheme [28] into the algorithm (54). The BGK algorithm with the GZS scheme is expressed as

$$f_i(\mathbf{x} + \mathbf{c}_i \delta t, t + \delta t) - f_i(\mathbf{x}, t) = -\frac{f_i(\mathbf{x}, t) - f_i^{eq}(\mathbf{x}, t)}{\tau} + F_i \delta t \quad (60)$$

where

$$F_i = \left(1 - \frac{1}{2\tau}\right) w_i \left[\frac{(\mathbf{c}_i - \mathbf{u})}{c_s^2} + \frac{(\mathbf{c}_i \cdot \mathbf{u})}{c_s^4} \mathbf{c}_i \right] \cdot \mathbf{F}_{ext}, \quad (61)$$

with

$$\sum_i^N F_i = 0, \quad \sum_i^N \mathbf{c}_i F_i = \left(1 - \frac{1}{2\tau}\right) \mathbf{F}_{ext}, \quad (62)$$

$$\sum_i^N \mathbf{c}_i \mathbf{c}_i F_i = \left(1 - \frac{1}{2\tau}\right) (\mathbf{u} \mathbf{F}_{ext} + \mathbf{F}_{ext} \mathbf{u}). \quad (63)$$

As pointed out by [9], the application of the Chapman-Enskog expansion analysis in (60) gives rise to the following expression

$$\sum_{i=1}^N \mathbf{c}_i \left[\frac{\partial f_i^{eq}}{\partial t} + \mathbf{c}_i \cdot \nabla \left(f_i^{eq} + \left(1 - \frac{1}{2\tau}\right) f_i^{(1)} + \frac{\delta t}{2} F_i \right) \right] = \mathbf{F}_{ext}, \quad (64)$$

where this time

$$f^{(1)} \simeq -\tau \delta t D_i f_i^{eq} + \tau \delta t F_i. \quad (65)$$

Follows that

$$\sum_{i=1}^N \mathbf{c}_i (\mathbf{c}_i \cdot \nabla f_i^{(1)}) \simeq -\sum_{i=1}^N \tau \delta t \mathbf{c}_i (\mathbf{c}_i \cdot \nabla (\mathbf{c}_i \cdot \nabla f_i^{eq})) + \tau \delta t \mathbf{c}_i (\mathbf{c}_i \cdot \nabla F_i). \quad (66)$$

Substituting (66) into (64), we obtain

$$\sum_{i=1}^N \mathbf{c}_i \left[\frac{\partial f_i^{eq}}{\partial t} + \mathbf{c}_i \cdot \nabla \left(f_i^{eq} - \left(\tau - \frac{1}{2} \right) \delta t (\mathbf{c}_i \cdot \nabla f_i^{eq}) + \tau \delta t F_i \right) \right] = \mathbf{F}_{ext}. \quad (67)$$

The extra term $\mathbf{c}_i(\mathbf{c}_i \cdot \nabla)\tau\delta t F_i$ is associated with the lattice discrete effects that only appears for variable forcing terms. For this term, the following discretization based on isotropic finite differences [29] can be considered

$$\sum_{i=1}^N \mathbf{c}_i(\mathbf{c}_i \cdot \nabla)\tau\delta t F_i \simeq \sum_{i=1}^N \frac{\tau}{2} \mathbf{c}_i [F_i(\mathbf{x} + \mathbf{c}_i\delta t, t) - F_i(\mathbf{x} - \mathbf{c}_i\delta t, t)]. \quad (68)$$

Therefore, the single-step algorithm for the velocity (55) should be rewritten as

$$\begin{aligned} \mathbf{u}(\mathbf{x}, t + \delta t) = & \frac{1}{\rho(\mathbf{x}, t + \delta t)} \sum_{i=1}^N \{ \mathbf{c}_i f_i^{eq}(\mathbf{x} - \mathbf{c}_i\delta t, t) + \\ & + (\tau - 1)[f_i^{eq}(\mathbf{x} + \mathbf{c}_i\delta t, t) - 2f_i^{eq}(\mathbf{x}, t) + f_i^{eq}(\mathbf{x} - \mathbf{c}_i\delta t, t)] \} - \\ & - \frac{\tau\delta t}{2} \mathbf{c}_i [F_i(\mathbf{x} + \mathbf{c}_i\delta t, t) - F_i(\mathbf{x} - \mathbf{c}_i\delta t, t)] + \\ & + \mathbf{F}_{ext}(\mathbf{x}, t)\delta t. \end{aligned} \quad (69)$$

With this improvement, it is possible to simulate more accurately multiple forms of external force interactions, including space- and time-dependent body forces, such as the Lorentz force [1]

$$\mathbf{F}_{Lorentz} = \mathbf{J} \times \mathbf{B} = (\nabla \times \mathbf{B}) \times \mathbf{B}, \quad (70)$$

where the curl can be calculated by using isotropic finite differences [29]. Effects of magnetic fields can also be introduced by changing the equilibrium distribution [4] in such a way that the divergence of the Maxwell stress tensor is implemented [4, 6]. This approach have not shown stable results in our numerical experiments for the case of non-uniform magnetic fields in simulations involving very small R_m . For this reason, in this article the forcing term approach is considered in all of the numerical experiments.

B. Boundary condition-enforced IBM

In this section, in order to introduce the effects of curved boundaries in MHD flows, we consider the immersed boundary method (IBM). In this method a fixed Eulerian mesh is applied in which the flow field is resolved, while the immersed solid boundary is described by a set of discrete Lagrangian points distributed in the fluid domain. The flow variables resolved on the Eulerian mesh are corrected by a restoration force exerted from the solid boundary [11]. In this article, we consider velocity and magnetic field corrections given by an extension of the boundary condition-enforced IBM based on the developments in [26], as we describe below.

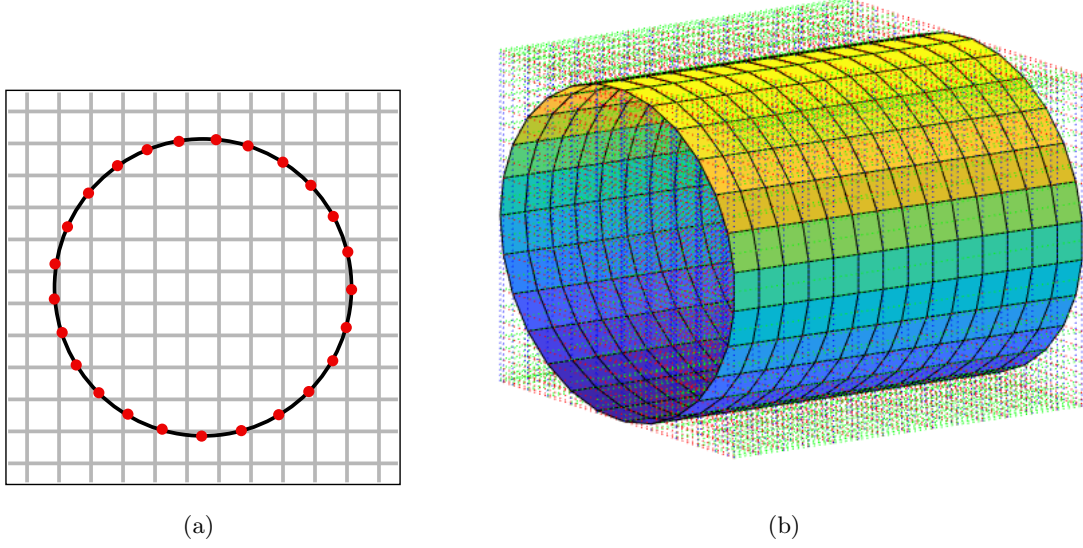


FIG. 3. (a) Cylinder with boundary markers (in red) positioned in the fluid domain. The Eulerian and the Lagrangian meshes are independent. (b) Schematic representation of the typical immersed boundary considered for the MHD pipe flows in this article.

In most of the IBM, the introduction of the effects of the boundaries is given by predictor-correction algorithm. In the predictor step, the LBM algorithm solves the following general system without boundary effects

$$\frac{\partial \rho}{\partial t} + \nabla \cdot (\rho \mathbf{u}) = 0 \quad (71)$$

$$\frac{\partial(\rho \mathbf{u})}{\partial t} + \nabla \cdot (\rho(\mathbf{u} \otimes \mathbf{u})) = -\nabla p + \nabla \cdot [\mu(\nabla \mathbf{u} + \nabla \mathbf{u}^T)] + \mathbf{F}_{ext}. \quad (72)$$

The effects of the boundaries are imposed as an extra forcing term introduced in the corrector step as

$$\frac{\partial(\rho \mathbf{u})}{\partial t} = \mathbf{f}, \quad (73)$$

where \mathbf{f} is determined by the IBMs to reproduce the effects of the immersed objects. Since the forcing term \mathbf{f} is not considered in the prediction step, the intermediate velocity \mathbf{u}^* obtained in the predictor step must be corrected. The corrector step (73) is discretized as

$$\rho \delta \mathbf{u} = \mathbf{f} \delta t, \quad (74)$$

where $\delta \mathbf{u}$ is the velocity correction. The corrected velocity is given by

$$\mathbf{u} = \mathbf{u}^* + \delta \mathbf{u}. \quad (75)$$

In order to calculate the corrections, interpolations between the Lagrangian and the Eulerian meshes are usually made using the discrete delta functions [11]. In this article, we consider a different approach for the interpolation procedure, which was suggested by [30] in the context of 2D flows. In this work, the authors showed that the use of Lagrange polynomials, instead of numerical delta functions, gives significantly better results in terms of accuracy. More specifically, the velocity correction $\delta \mathbf{u}(\mathbf{x}_i)$ at Eulerian mesh cell i is distributed from the velocity corrections $\delta \mathbf{U}(\mathbf{X}_j)$ at Lagrangian points \mathbf{X}_j by [30] using classical Lagrangian interpolation schemes given by

$$\delta \mathbf{u}(\mathbf{x}_i) = \sum_{j=1}^N D(\mathbf{x}_i - \mathbf{X}_j) \delta \mathbf{U}(\mathbf{X}_j), \quad (76)$$

and

$$\mathbf{u}(\mathbf{x}_i) = \sum_{j=1}^N D(\mathbf{x}_i - \mathbf{X}_j) \mathbf{U}(\mathbf{X}_j), \quad (77)$$

where N is the total number of Lagrangian points and D is accounts for a Lagrange velocity polynomial interpolation written as

$$D(\mathbf{r}) = D_x(r_x) D_y(r_y) D_z(r_z), \quad (78)$$

where, for the purposes of this article, the coefficients are given by

$$D_x(r_x) = \begin{cases} \frac{1}{2}(r_x + 1)(r_x + 2), & \text{for } r_x \in [-3/2, -1/2], \\ 1 - r_x^2, & \text{for } r_x \in [-1/2, 1/2], \\ \frac{1}{2}(r_x - 1)(r_x - 2), & \text{for } r_x \in [1/2, 3/2], \end{cases} \quad (79)$$

and analogously for $D_y(r_y)$ and $D_z(r_z)$. The use higher order Lagrange polynomials is possible [30], but in the experiments of this article no significant differences were found by using them.

Analogously, the velocity $\mathbf{U}_b(\mathbf{X}_j)$ at the Lagrangian point \mathbf{X}_j can be interpolated from the corrected velocity \mathbf{u} at the Eulerian mesh points by using

$$\mathbf{U}_b(\mathbf{X}_j) = \sum_{i \in S(j)} D(\mathbf{x}_i - \mathbf{X}_j) \mathbf{u}(\mathbf{x}_i), \quad (80)$$

where $S(j)$ is the set of neighboring Eulerian cells near the Lagrangian point \mathbf{X}_j defined as

$$S(j) = \left\{ i, \left| \frac{x_i - X_j}{h} \right|, \left| \frac{y_i - Y_j}{h} \right|, \left| \frac{z_i - Z_j}{h} \right| \leq 2 \right\}, \quad (81)$$

where h is the grid spacing in the Eulerian mesh, which in this article is set to the unity without loss of generality. Substituting (76) and (75) into (80), we obtain the following equation

$$\mathbf{U}_b(\mathbf{X}_j) = \sum_{i \in S(j)} D(\mathbf{x}_i - \mathbf{X}_j) \mathbf{u}^*(\mathbf{x}_i) + \sum_{i \in S(j)} D(\mathbf{x}_i - \mathbf{X}_j) \sum_{j=1}^N D(\mathbf{x}_i - \mathbf{X}_j) \delta \mathbf{U}(\mathbf{X}_j), \quad (82)$$

where $\delta\mathbf{U}(\mathbf{X}_j)$ is an unknown velocity correction, \mathbf{U}_b is an imposed velocity on the immersed boundary points and \mathbf{u}^* is known from the predictor step. In a matrix form the relation (82) is given by

$$\mathbf{U}_b = \mathbf{D}\mathbf{u}^* + \mathbf{D}\mathbf{D}^T\delta\mathbf{U}, \quad (83)$$

where

$$\mathbf{U}_b = \begin{bmatrix} \mathbf{U}_b(\mathbf{X}_1) \\ \vdots \\ \mathbf{U}_b(\mathbf{X}_N) \end{bmatrix}, \quad \mathbf{u}^* = \begin{bmatrix} \mathbf{u}^*(\mathbf{x}_1) \\ \vdots \\ \mathbf{u}^*(\mathbf{x}_M) \end{bmatrix}, \quad \delta\mathbf{U} = \begin{bmatrix} \delta\mathbf{U}(\mathbf{X}_1) \\ \vdots \\ \delta\mathbf{U}(\mathbf{X}_N) \end{bmatrix}, \quad (84)$$

$$\mathbf{D} = \begin{bmatrix} D(\mathbf{x}_1 - \mathbf{X}_1) \dots D(\mathbf{x}_M - \mathbf{X}_1) \\ \vdots \quad \ddots \quad \vdots \\ D(\mathbf{x}_1 - \mathbf{X}_N) \dots D(\mathbf{x}_M - \mathbf{X}_N) \end{bmatrix}. \quad (85)$$

where M is the total number of Eulerian points the sets $S(j)$, $j = 1, \dots, N$. The velocity correction $\delta\mathbf{U}$ is obtained by solving the system

$$\mathbf{A}\delta\mathbf{U} = \mathbf{b}, \quad (86)$$

where $\mathbf{A} = \mathbf{D}\mathbf{D}^T \in \mathbb{R}^N \times \mathbb{R}^N$ and $\mathbf{b} = \mathbf{U}_b - \mathbf{D}\mathbf{u}^*$. The corresponding corrected velocity at the Eulerian nodes is given by

$$\mathbf{u} = \mathbf{u}^* + \delta\mathbf{u} = \mathbf{u}^* + \mathbf{D}^T\delta\mathbf{U}. \quad (87)$$

It is important to mention that the matrices \mathbf{D} and \mathbf{D}^T are easily obtained but the inversion of a matrix \mathbf{A} can be a non-trivial procedure. In the next, based on the developments in [26], we discuss an explicit strategy to solve the problem (86) which does not involve the direct inversion of the matrix \mathbf{A} .

C. Explicit boundary condition-enforced IBM

In a more explicit way, the system (86) is given by

$$\sum_j A_{ij} \delta\mathbf{U}(\mathbf{X}_j) = \mathbf{b}_i, \quad (88)$$

where

$$A_{ij} = \sum_k D(\mathbf{x}_k - \mathbf{X}_i) D(\mathbf{x}_k - \mathbf{X}_j). \quad (89)$$

Note that we only need to consider the non-zero values of the coefficients A_{ij} , i.e., in the summation in (88) we only need consider $j \in \{A_{ij} \neq 0\}$. The momentum correction is then linearized in the vicinity of \mathbf{X}_i in the following form

$$\delta \mathbf{U}(\mathbf{X}_j) = \delta \mathbf{U}(\mathbf{X}_i) + \frac{\partial \delta \mathbf{U}}{\partial \mathbf{X}}(\mathbf{X}_i) d\mathbf{X}_{ij} + O(\|d\mathbf{X}_{ij}\|^2), \quad (90)$$

where $d\mathbf{X}_{ij} = \mathbf{X}_j - \mathbf{X}_i$. Assuming that the curvature of the immersed boundary is small in such a way it can be approximated by a straight wall in the vicinity of \mathbf{X}_i [13, 26], it follows that

$$\sum_j A_{ij} \frac{\partial \delta \mathbf{U}}{\partial \mathbf{X}}(\mathbf{X}_i) d\mathbf{X}_{ij} \simeq 0, \quad (91)$$

as a consequence of the properties of the interpolating function (79). Substituting (90) and (91) into (88), we have

$$\sum_j A_{ij} \delta \mathbf{U}(\mathbf{X}_i) = \mathbf{b}_i, \quad (92)$$

up to a second order error. Now note that the unknown correction $\delta \mathbf{U}(\mathbf{X}_i)$ can now be moved out of the summation, which leads to the simplified system [26]

$$\delta \mathbf{U}(\mathbf{X}_i) \sum_j A_{ij} = \mathbf{b}_i, \quad (93)$$

or in a matrix form

$$\begin{bmatrix} \ddots & \mathbf{0} & \mathbf{0} \\ \mathbf{0} & d_i & \mathbf{0} \\ \mathbf{0} & \mathbf{0} & \ddots \end{bmatrix} \delta \mathbf{U} = \mathbf{b}. \quad (94)$$

where

$$d_i = \sum_{j \in \{A_{ij} \neq 0\}} A_{ij}, \quad i = 1, \dots, N. \quad (95)$$

where N is the number of the immersed boundary points. Substituting the solutions of (94) into (87), follows that the corrected velocities in the Eulerian nodes is given by

$$\mathbf{u} = \mathbf{u}^* + \mathbf{D}^T \delta \mathbf{U} = \mathbf{u}^* + \mathbf{D}^T \begin{bmatrix} \ddots & \mathbf{0} & \mathbf{0} \\ \mathbf{0} & \frac{1}{d_i} & \mathbf{0} \\ \mathbf{0} & \mathbf{0} & \ddots \end{bmatrix} \mathbf{b}. \quad (96)$$

An interesting feature of this method is that it avoids the direct inversion of the matrix \mathbf{A} in (86), which can be computationally expensive, specially if moving boundaries are involved, which requires the inversion of \mathbf{A} repeatedly. The explicit character of (96) also simplifies the implementation of the method on GPUs.

D. Explicit boundary condition-enforced IBM for magnetic field

In a analogous way, the introduction of the effects of Dirichlet boundary conditions are introduced in the equations for the magnetic field by considering a similar predictor-correction algorithm, where the intermediate flow variables obtained in the predictor step are then corrected by the IBMs in the subsequent corrector step. In the predictor step, we solve the system

$$\frac{\partial \mathbf{B}}{\partial t} + \nabla \cdot (\mathbf{u}\mathbf{B} - \mathbf{B}\mathbf{u}) = \eta \nabla^2 \mathbf{B} + \mathbf{Q}, \quad (97)$$

$$\nabla \cdot \mathbf{B} = 0. \quad (98)$$

where \mathbf{Q} denotes a general source term. In this method, the boundary effects are imposed as an extra source term introduced in following corrector step

$$\frac{\partial \mathbf{B}}{\partial t} = \mathbf{q}, \quad (99)$$

where \mathbf{q} is determined by the IBMs to include the effects of the magnetic fields generated by immersed objects. The corrector-step is discretized as

$$\delta \mathbf{B} = \mathbf{q} \delta t, \quad (100)$$

and the corresponding corrected magnetic field will be given by

$$\mathbf{B} = \mathbf{B}^* + \delta \mathbf{B}, \quad (101)$$

where \mathbf{B}^* is the magnetic field obtained in the predictor step (97). Following the same steps as in the case involving the velocity field, it follows that

$$\mathbf{B} = \mathbf{B}^* + \mathbf{D}^T \begin{bmatrix} \cdot \cdot & \mathbf{0} & \mathbf{0} \\ \mathbf{0} & \frac{1}{d_i} & \mathbf{0} \\ \mathbf{0} & \mathbf{0} & \cdot \cdot \end{bmatrix} (\mathbf{B}_b - \mathbf{D}\mathbf{B}^*), \quad (102)$$

where \mathbf{B}_b is the imposed magnetic field on the immersed boundary points.

The use of the corrections (96) and (102) gives accurate results if coupled with the single-step algorithm (54) when the magnetic Prandtl number Pr_m is closer to 1. For smaller values of Pr_m , some problems appears, as we can see in the Figure 4, where we performed simulations of two MHD flows using the algorithms (54) and (55) with $Pr_m = 0.1$ and $Ha = 18$ in a computational grid with size $n_x \times n_y \times n_z = 5 \times 80 \times 80$. The immersed boundary is approximated by a cylinder formed by small rectangular (almost squared) elements, as shown in Figure 3(b). The number of elements is chosen in such a way that each element has an area close to $(\delta x)^2$, which is a common criterion for IB methods [11]. It is possible to see a significant mismatch in the comparisons between the numerical solutions for U_x and B_x and the Gold's solutions (56) and (57). A similar mismatch also appears in the quasi-static regime as shown in Figure 5, where a simulation with $Pr_m = 4 \times 10^{-7}$ and $Ha = 18$ with the same computational grid size is performed using some methods to be described in the next sections. All this suggests that the accuracy of the corrections given by (96) and (102) have some dependence with respect to the coefficients of viscosity and resistivity. It implies that for the simulations of the quasi-static approximation characterized by $Pr_m \ll 1$, some improvements are needed. Strategies for the solution of this problem will be described in the next subsections.

E. Viscosity-independent boundary condition-enforced IBM

In this section, we extend the previous results for IBM developed for the case where we present arbitrary magnetic Reynolds number. In [13], the authors suggested that the complete description of an immersed boundary problem also involves the inclusion of non-dimensional IB force. More specifically, in any physical configuration, the flow solution can be described by a set of non-dimensional physical quantities, as the non-dimensional pressure and velocity

$$\mathbf{u}^* = \frac{\mathbf{u}}{U_r} \quad p^* = \frac{p - p_r}{\rho_r U_r^2}, \quad (103)$$

where U_r , p_r and ρ_r are velocity, pressure and density of reference, respectively. In addition, a non-dimensional IB force is defined as

$$\mathbf{f}^* = \frac{\mathbf{f}D}{\rho_r U_r^2}. \quad (104)$$

Consider two sets of dimensional quantities $(\rho_1, \mathbf{u}_1, \mathbf{f}_1)$ and $(\rho_2, \mathbf{u}_2, \mathbf{f}_2)$, which we call systems 1 and 2 respectively. Let us also consider that the reference densities and characteristic lengths are

the same, i.e., $\rho_1 = \rho_2 = \rho_r$ (small Mach numbers assumption) and $L_1 = L_2$. In this situation, if the both systems are solutions of the same physical problem, then the sets 1 and 2 results in the same set of non-dimensional quantities, which in our case implies in the same Reynolds, same Mach and same Froude numbers. In this case, denoting the reference velocities of the systems 1 and 2 by U_1 and U_2 respectively, it follows that the two systems are connected by the scaling factor defined as $\lambda = U_2/U_1$, which is also the viscosity ratio between configurations 1 and 2, i.e., $\lambda = \nu_2/\nu_1$. As a consequence, the following scaling laws are verified

$$\mathbf{u}_1 = \frac{1}{\lambda} \mathbf{u}_2, \quad \mathbf{f}_1 = \frac{1}{\lambda^2} \mathbf{f}_2. \quad (105)$$

The IB forces can be rewritten as

$$\mathbf{f}_1 = \rho_r \delta \mathbf{u}_2 = \rho_r (\mathbf{u}_1 - \mathbf{u}_1^*), \quad \mathbf{f}_2 = \rho_r \delta \mathbf{u}_2 = \rho_r (\mathbf{u}_2 - \mathbf{u}_2^*), \quad (106)$$

which leads to the the following equation

$$\mathbf{u}_1^* = \left(\frac{1}{\lambda} - \frac{1}{\lambda^2} \right) \mathbf{u}_2 + \frac{1}{\lambda^2} \mathbf{u}_2^*. \quad (107)$$

Comparing (105) and (107), we can observe that despite the fact that the physical quantities (105) exhibit self-similar scaling properties, the velocities corrected by the IBM cannot be directly rescaled using λ , because \mathbf{u}_1^* has a dependence on \mathbf{u}_2 . This property is one of the possible causes of the error shown in Figure 4. In the following, we describe the proper corrections that should be considered in order to introduce the correct IB adjustments.

Let us denote the Lagrangian velocity corrections given by (96) for the systems 1 and 2 as $\delta \mathbf{U}_1$ and $\delta \mathbf{U}_2$ respectively. The scaling verified in the Eulerian nodes should also be verified in the Lagrangian nodes, i.e., $\delta \mathbf{U}_2 = \lambda^2 \delta \mathbf{U}_1$. Let us consider that the system 1 is a reference configuration that does not need scaling corrections. Using (86) it follows that

$$\mathbf{D} \mathbf{D}^T \delta \mathbf{U}_1 = \mathbf{U}_{b,1} - \mathbf{D} \mathbf{u}_1^*. \quad (108)$$

As we already mentioned, the matrix $\mathbf{D} \mathbf{D}^T$ is usually ill-conditioned and its inversion is a non-trivial procedure, requiring some special techniques in order to approximate the inversion of $\mathbf{D} \mathbf{D}^T$. Let us consider, without loss of generality, the least square solution of (108) written in terms of the pseudoinverse $(\mathbf{D} \mathbf{D}^T)^\dagger$ with the representation formula given by

$$\delta \mathbf{U}_1 = (\mathbf{D} \mathbf{D}^T)^\dagger (\mathbf{U}_{b,1} - \mathbf{D} \mathbf{u}_1^*), \quad (109)$$

and then

$$\delta \mathbf{U}_2 = \lambda^2 (\mathbf{D} \mathbf{D}^T)^\dagger (\mathbf{U}_{b,1} - \mathbf{D} \mathbf{u}_1^*). \quad (110)$$

Using (105) and (107), it follows that from (110) we can derive

$$\delta \mathbf{U}_2 = (\mathbf{D}\mathbf{D}^T)^\dagger (\lambda \mathbf{U}_{b,2} + (1 - \lambda)(\mathbf{D}\mathbf{u}_2 - \mathbf{D}\mathbf{u}_2^*)). \quad (111)$$

Using (96), we obtain

$$\mathbf{u}_2 = \mathbf{u}_2^* + \mathbf{D}^T \delta \mathbf{U}_2, \quad (112)$$

and finally, the IB force verifying the correct scaling properties will be given by

$$\begin{aligned} \delta \mathbf{U}_2 &= \lambda (\mathbf{D}\mathbf{D}^T)^\dagger (\mathbf{U}_{b,2} - \mathbf{D}\mathbf{u}_2^*) + (1 - \lambda) (\mathbf{D}\mathbf{D}^T)^\dagger \mathbf{D}\mathbf{D}^T \delta \mathbf{U}_2. \\ &= \lambda (\mathbf{D}\mathbf{D}^T)^\dagger (\mathbf{U}_{b,2} - \mathbf{D}\mathbf{u}_2^*) + (1 - \lambda) \mathbf{D}\mathbf{D}^\dagger \delta \mathbf{U}_2, \end{aligned} \quad (113)$$

where in the last equation we consider some general properties of pseudo-inverse matrices [31]. It is important to observe that the term $\mathbf{D}\mathbf{D}^\dagger$ does not have to be the general identity matrix \mathbf{I} . Depending on the immersed boundary method, we may cancel the coefficient λ , but for some explicit velocity correction-based IBM, as the one described in this article, that is not the case.

Due to the properties of the interpolating functions (79), it follows that we can use power series and show that one first approximation for \mathbf{D}^\dagger is given by \mathbf{D}^T [31–33]. Using again (94) and considering $\mathbf{D}^\dagger \simeq \mathbf{D}^T$, we obtain

$$\mathbf{D}\mathbf{D}^\dagger \delta \mathbf{U}_2 \simeq \mathbf{D}\mathbf{D}^T \delta \mathbf{U}_2 \simeq \begin{bmatrix} \ddots & \mathbf{0} & \mathbf{0} \\ \mathbf{0} & d_i & \mathbf{0} \\ \mathbf{0} & \mathbf{0} & \ddots \end{bmatrix} \delta \mathbf{U}_2. \quad (114)$$

Consequently, we can rewrite (113) as

$$\delta \mathbf{U}_2 = \begin{bmatrix} \ddots & \mathbf{0} & \mathbf{0} \\ \mathbf{0} & \frac{\lambda}{1+d_i(\lambda-1)} & \mathbf{0} \\ \mathbf{0} & \mathbf{0} & \ddots \end{bmatrix} (\mathbf{D}\mathbf{D}^T)^\dagger (\mathbf{U}_{b,2} - \mathbf{D}\mathbf{u}_2^*), \quad (115)$$

where the term $(\mathbf{D}\mathbf{D}^T)^\dagger (\mathbf{U}_{b,2} - \mathbf{D}\mathbf{u}_2^*)$ in (115) corresponds to the previous velocity correction obtained by finding the least-square solution of the system (86). It is interesting to note that the form of the scalings in the matrix in the equation (115) is very similar to the scalings obtained in [13] in the context of the direct forcing IBM, with the difference that in our work we found a matrix of scalings rather than a single scaling.

Then, substituting (115) into (112) and using (94), it follows that the new corrected velocity, considering the necessary scaling corrections, is be given by

$$\mathbf{u}_2 = \mathbf{u}_2^* + \mathbf{D}^T \begin{bmatrix} \ddots & \mathbf{0} & \mathbf{0} \\ \mathbf{0} & \frac{\lambda}{d_i(1+d_i(\lambda-1))} & \mathbf{0} \\ \mathbf{0} & \mathbf{0} & \ddots \end{bmatrix} \mathbf{b}. \quad (116)$$

In the next subsection, we consider the introduction of similar corrections in the context of the explicit boundary condition-enforced IBM for the magnetic field equations.

F. Resistivity-independent boundary condition-enforced IBM

In this subsection, for the explicit IBM for the magnetic field described in the Subsection VD, we consider a procedure analogous to the case involving the velocity field. In this case, the two non-dimensional important physical parameters in this case are

$$R_m = \frac{U_0 L}{\eta}, \quad Ha = \frac{B_0 L}{\sqrt{\eta \nu}}. \quad (117)$$

Consider two sets of dimensional quantities $(\mathbf{u}_1, \mathbf{B}_1)$ and $(\mathbf{u}_2, \mathbf{B}_2)$, which we also call systems 1 and 2 respectively. We also assume that the both sets are associated with the same physical system, which implies in the same set of non-dimensional quantities. The corresponding scaling factor will be given by $\lambda_{mag} = \eta_2/\eta_1$, which leads to the following relationships

$$\mathbf{B}_1 = \frac{1}{\lambda_{mag}} \mathbf{B}_2, \quad \mathbf{q}_1 = \frac{1}{\lambda_{mag}^2} \mathbf{q}_2, \quad (118)$$

and similarly

$$\mathbf{B}_1^* = \left(\frac{1}{\lambda_{mag}} - \frac{1}{\lambda_{mag}^2} \right) \mathbf{B}_2 + \frac{1}{\lambda_{mag}^2} \mathbf{B}_2^*, \quad (119)$$

where \mathbf{B}_1^* and \mathbf{B}_2^* are magnetic fields obtained in the predictor step (97). The equation for the corrected magnetic field \mathbf{B}_2 is then given by

$$\mathbf{B}_2 = \mathbf{B}_2^* + \mathbf{D}^T \begin{bmatrix} \ddots & \mathbf{0} & \mathbf{0} \\ \mathbf{0} & \frac{\lambda_{mag}}{d_i(1+d_i(\lambda_{mag}-1))} & \mathbf{0} \\ \mathbf{0} & \mathbf{0} & \ddots \end{bmatrix} (\mathbf{B}_{2,b} - \mathbf{D} \mathbf{B}_2^*), \quad (120)$$

where $\mathbf{B}_{2,b}$ is the imposed magnetic field on the immersed boundary points associated to the system configuration 2.

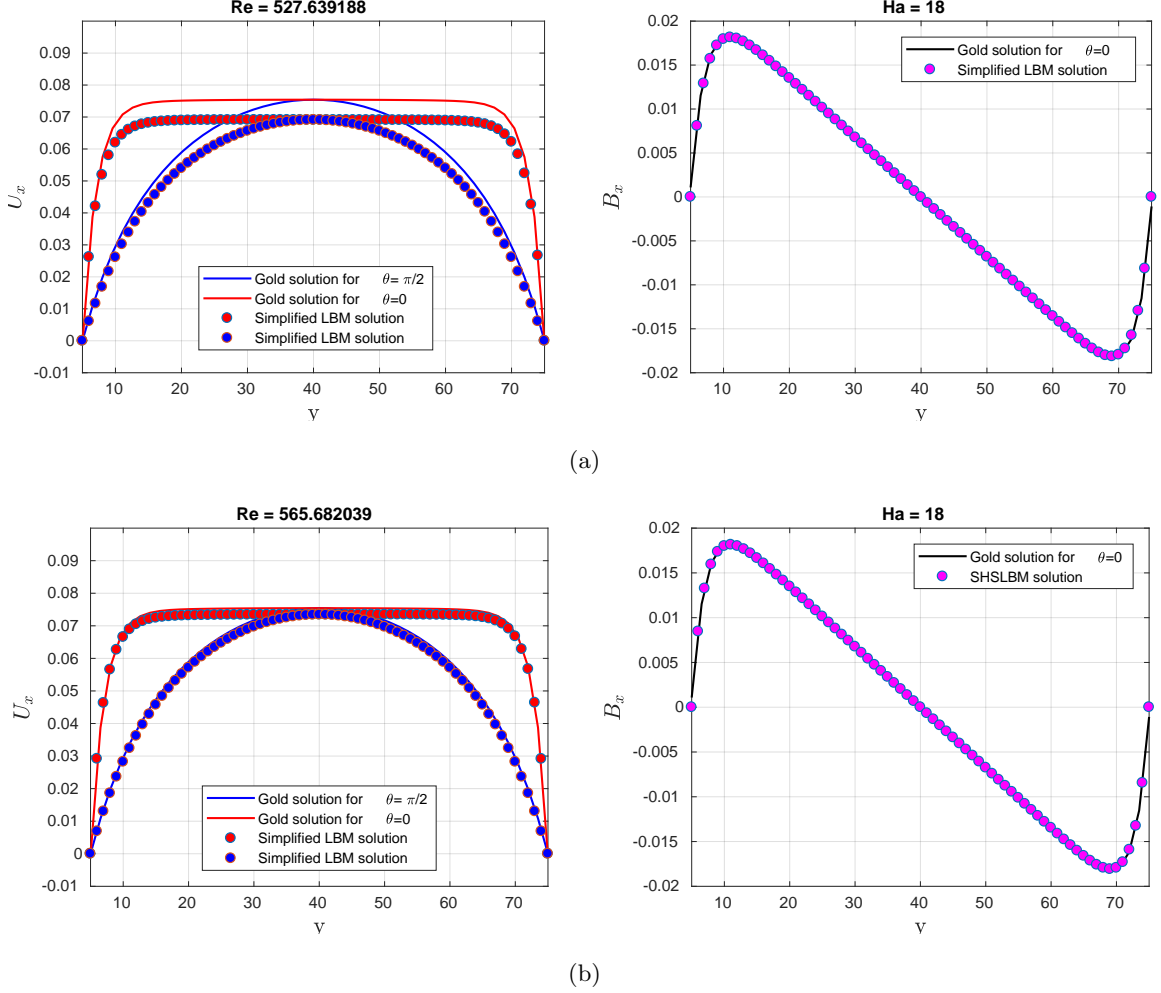


FIG. 4. Simulation of MHD pipe flows under the presence of a transversal magnetic field with viscosity $\nu = 0.004$, resistivity $\eta = 0.04$ and $Ha = 18$. In these experiments, we show the magnetic and velocity field profiles for a simulation with pipe radius $r = 35$ and constant pressure difference $\frac{\partial p}{\partial x} = -3.7 \times 10^{-5}$, and we compare with the respective analytical solutions given by (56) and (57). In (a) we consider the corrections given by (96) and (102). In (b) we consider the new corrections given by (116) and (120) showing a much better agreement with the Gold's analytical solutions.

An application of the new velocity and magnetic fields corrections by the formulas (116) and (120) is shown in Figure 4, where we performed simulations of two MHD flows using the algorithms (54) and (55) with $Pr_m = 0.1$ and $Ha = 18$. With the new corrections, we can observe a much better verification of the Gold's solutions (56) and (57).

G. Stability improvements for high values of viscosity and resistivity

In this section, we aim to extend range of stability of the previous simplified methods for regimes associated with high values of relaxation times. The main idea is first to set the relaxation time $\tau = 1$ [14, 34] in the classical BGK algorithm (15) obtaining the so-called macroscopic lattice Boltzmann model given simply by

$$\rho(\mathbf{x}, t) = \sum_{\alpha} f_{\alpha}^{eq}(\mathbf{x} - \mathbf{c}_i \delta t, t - \delta t), \quad (121)$$

$$\mathbf{u}(\mathbf{x}, t) = \frac{1}{\rho(\mathbf{x}, t)} \sum_{\alpha} \mathbf{c}_{\alpha} f_{\alpha}^{eq}(\mathbf{x} - \mathbf{c}_i \delta t, t - \delta t). \quad (122)$$

It is possible to show that the particle speed c can be changed in such a way to include the effects of different viscosities ν as

$$c = \frac{6\nu}{\delta x}, \quad (123)$$

where $\delta t = \delta x/c$. In our applications, for the sake of simplicity, we always consider $\delta x = 1$. Accordingly, the change in the particle speed c also implies in the following changes in the lattice velocities of the D3Q27 scheme as

$$\mathbf{c}_x = (0, -c, 0, 0, -c, -c, -c, -c, 0, 0, -c, -c, -c, -c, c, 0, 0, c, c, c, 0, 0, c, c, c, c)^T, \quad (124)$$

$$\mathbf{c}_y = (0, 0, -c, 0, -c, c, 0, 0, -c, -c, -c, -c, c, c, 0, c, 0, c, -c, 0, 0, c, c, c, c, -c, -c)^T, \quad (125)$$

$$\mathbf{c}_z = (0, 0, 0, -c, 0, 0, -c, c, -c, c, -c, c, -c, c, 0, 0, c, 0, 0, c, -c, c, -c, c, -c, c, -c)^T. \quad (126)$$

The algorithm formed by (121) and (122) is particularly efficient and stable for flow simulations with small and moderate Reynolds numbers. High Reynolds numbers usually will require a very small δx , which implies in a substantial increase of the number of points in the computational grid. In this article, this algorithm is suggested as an extension for $\tau \geq 1$ of the single-step algorithm (54). Actually, it can be considered an extension for any other simplified method that also have problems for high values of relaxation times.

In this article, we also extend the idea of the macroscopic LBM algorithm for the magnetic field equations (3) and (4). Substituting $\tau_m = 1$ in (38), we obtain the following algorithm

$$\begin{aligned} B_x(\mathbf{x}, t) &= \sum_i g_{xi}^{eq}(\mathbf{x} - \mathbf{c}_i \delta t, t - \delta t), \\ B_y(\mathbf{x}, t) &= \sum_i g_{yi}^{eq}(\mathbf{x} - \mathbf{c}_i \delta t, t - \delta t), \\ B_z(\mathbf{x}, t) &= \sum_i g_{zi}^{eq}(\mathbf{x} - \mathbf{c}_i \delta t, t - \delta t). \end{aligned} \quad (127)$$

Recall the formula for the resistivity η as a function of the relaxation time τ_m given by

$$\eta = c_s^2 \left(\tau_m - \frac{1}{2} \right) \delta t = \frac{c^2}{3} \left(\tau_m - \frac{1}{2} \right) \delta t. \quad (128)$$

Introducing $\tau_m = 1$ in (128), we obtain

$$\eta = \frac{c^2}{6} \delta t = \frac{c}{6} \delta x = \frac{(\delta x)^2}{6 \delta t}, \quad (129)$$

and considering $\delta x = 1$, we have $\eta = c/6$.

The algorithm given by (127) solves (3) and (4) for a wide range of η values, but similarly to the algorithm given by (121) and (122) for the velocity field, this algorithm is not practical for small values of resistivity, but is very suitable for the values of resistivity associated with the quasi-static approximation (7). The idea in this article is to set the $\delta x = 1$ in (129) (velocity and magnetic fields are solved in the same computational grid) and obtain $\delta t = 1/6\eta$. It implies that if $\eta > 1/6$, then the algorithm (127) should be iterated a few times before every update of the single-step algorithm given by (54) and (55) for the momentum equation. The number of iterations N_{mag} for the algorithm (127) can be defined as

$$N_{mag} = \left\lceil \frac{1}{\delta t} \right\rceil, \quad (130)$$

where the function $\lceil \cdot \rceil$ denotes the smallest integer number greater or equal to $1/\delta t$. In many applications, very high values of resistivity generate a prohibitive value of N_{mag} , but in this situations we can work with some kind of effective number of iterations, as we shown in details in the Section V H. The result of this strategies is shown in Figures 6 and 7.

For a significant high values of η , the algorithm given by (127) converges to the equation

$$\eta \nabla^2 \mathbf{B} = \nabla \cdot (\mathbf{u} \mathbf{B} - \mathbf{B} \mathbf{u}). \quad (131)$$

as a natural asymptotic limit. A verification of the proposed single-step algorithm is shown in Figure 6, where a pipe flow submitted to a uniform transverse magnetic field is implemented for three different values of Hartmann numbers, $Ha = 12, 18$ and 24 , with $\eta = 10000$ and $\nu = 0,04$. Periodic boundary conditions are considered in the streamwise directions with Dirichlet boundary conditions at the walls of the pipe. All the simulations are initialized from zero velocity. The numerical solutions are compared with the Gold's solutions given by (56) and (57) for the values of $\theta = 0$ and $\theta = \pi/2$, showing a good agreement. In Figure 7, we analyze in more details the simulation with $Ha = 18$, showing that the solution not only verifies the Gold's solution, but also the initial transient regime accurately verifies the energy balance given by (58).

For most of the experiments in this article, we set $Ha = 18$, which we consider a representative value for the simulations with Hartman numbers between 1 and 30, in the sense that no significant differences have been verified by changing the values of Ha in this range. For higher values of Hartman numbers, grid refinements, especially close to the boundaries may be needed to handle the intensification of the Hartman layers [5], for example.

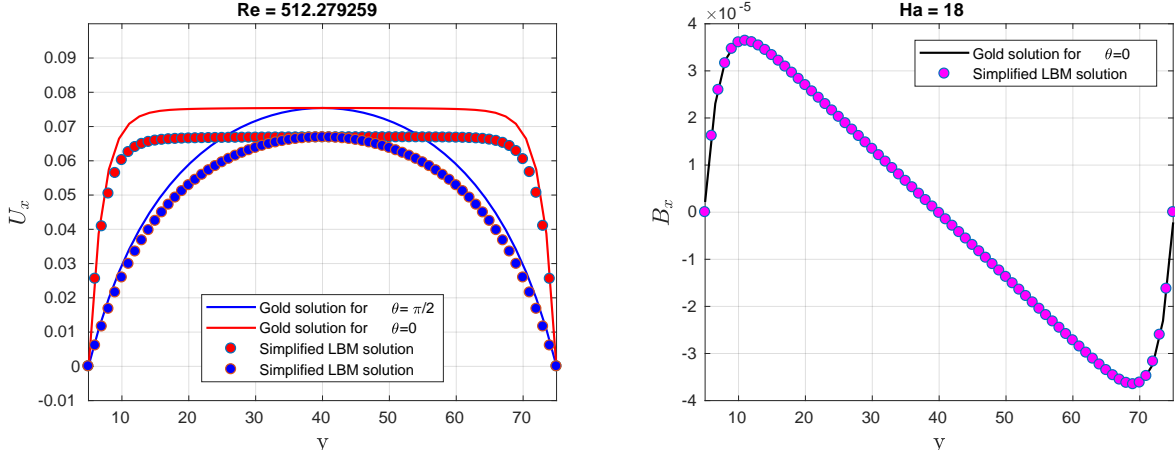


FIG. 5. Comparison with the Gold's solutions by using the single-step LBM algorithms given by (54) and (127) with viscosity $\nu = 0,004$, resistivity $\eta = 10000$ and Hartman number $Ha = 18$ in a pipe with radius $r = 35$. The algorithm for the magnetic field is iterated $N_{mag} = 12$ times before every update of the velocity field. The resulting magnetic Prandtl number $Pr_m = 4 \times 10^{-7}$. In this simulation, we consider the immersed boundary corrections given by (96) and (102). It is possible to observe a significant mismatch between analytical and numerical solutions, which is corrected by the introduction of the new corrections (116) and (120), as shown in Figures 6 and 7.

In the references [5, 7], the authors consider the introduction of extra parameters χ and γ and use the traditional BGK algorithm (38) to solve the following equation

$$\frac{\partial \mathbf{B}}{\partial t} + \frac{\chi}{\gamma} \nabla \cdot (\mathbf{u} \mathbf{B} - \mathbf{B} \mathbf{u}) = \frac{\eta}{\gamma} \nabla^2 \mathbf{B}, \quad (132)$$

which has a stationary solution given by

$$\nabla \cdot (\mathbf{u} \mathbf{B} - \mathbf{B} \mathbf{u}) = \frac{\eta}{\chi} \nabla^2 \mathbf{B}. \quad (133)$$

The parameter χ can be set to archive the desired magnetic Prandtl number Pr_m and the parameter γ , usually much smaller than 1, helps to increase the convergence rate to steady state solutions. The same strategy can also be applied for the single-step algorithm (54) as well. Originally in [5], this procedure is mostly considered for steady states solutions, but its applicability for general flow

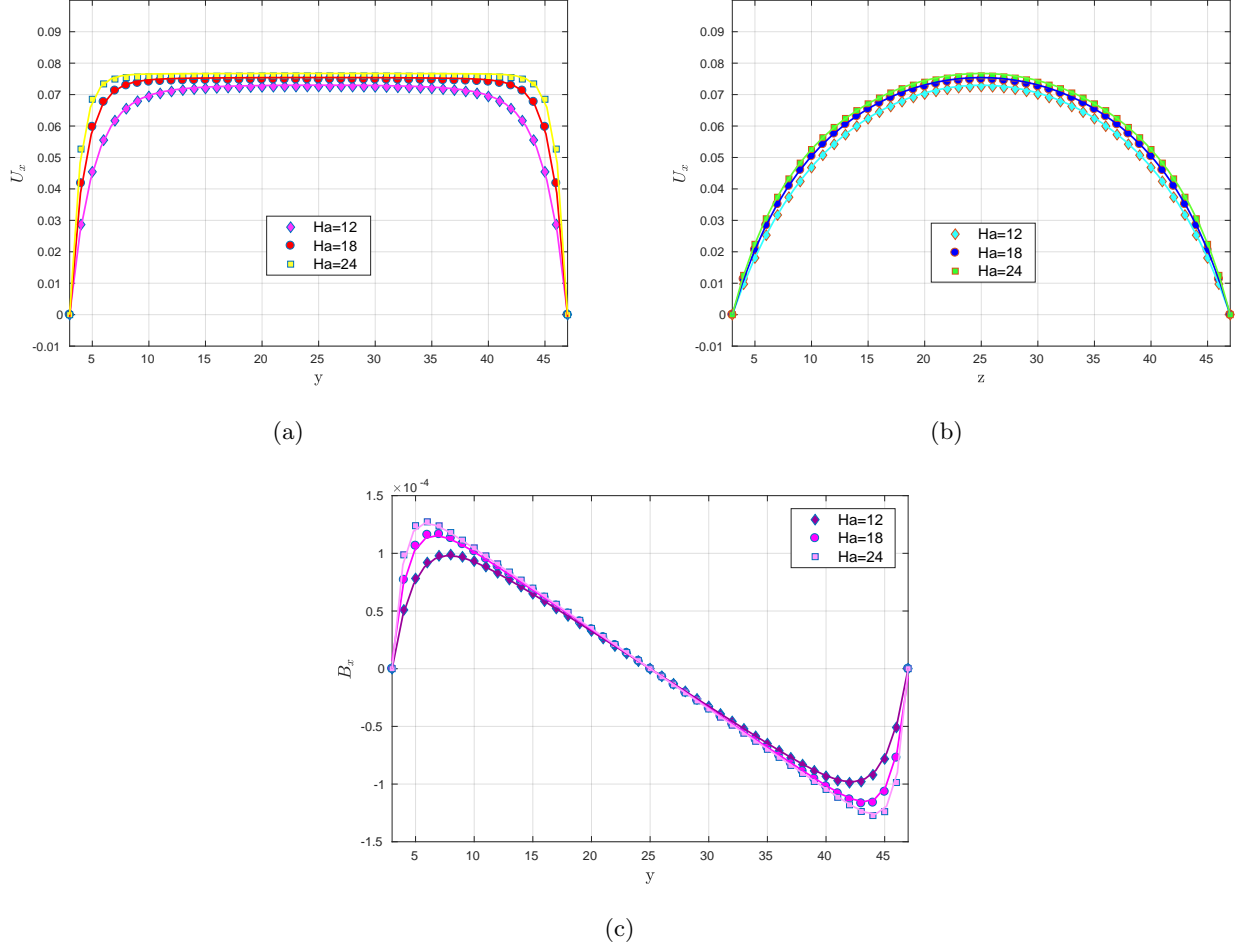


FIG. 6. Simulation of a MHD pipe flow submitted to a constant transverse magnetic field with a pipe radius $r = 22$, resistivity $\eta = 10000$ and viscosity $\nu = 0.04$. The results for three different values of Hartman $Ha = 12, 18$ and 24 are shown. In picture (a), the velocity profiles corresponding to the Gold's solution for $\theta = \pi/2$; in picture (b), the solutions corresponding to $\theta = 0$, and in (c), the magnetic field profiles for $\theta = \pi/2$. The continuous lines are the respective analytical solutions for each value of Ha .

regimes with $R_m \ll 1$ is not clear. In this article, the algorithm (127) gives a more direct route towards simulations with very small R_m with a much simpler and stable algorithm, and without the need of the introduction of extra parameters.

H. Strategies for very high values of resistivity

The formula (130) gives the necessary number of iterations for the convergence of the algorithm (127). Naturally, if the value of the resistivity is too high, the number of iterations becomes

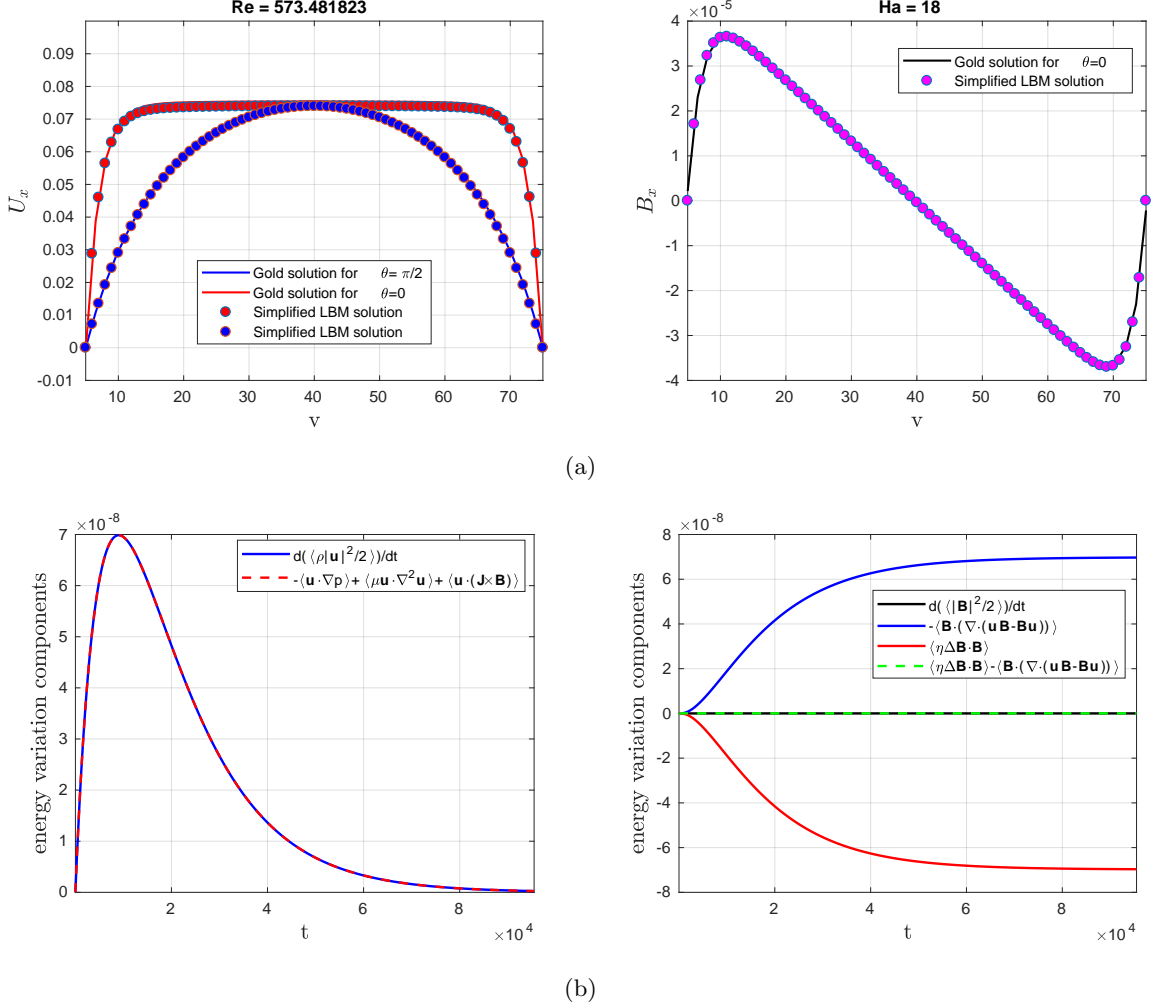


FIG. 7. Verification of the Gold's solutions by using the single-step LBM algorithms given by (54), (55) and (127), with viscosity $\nu = 0,004$, resistivity $\eta = 10000$ and Hartman number $Ha = 18$. The simulation is performed in a pipe with radius $r = 35$. The resulting magnetic Prandtl number equal to $Pr_m = 4 \times 10^{-7}$. In (a) we show the velocity and magnetic field profiles verifying the Gold's solutions (56) and (57), and in (b), we show the verification of the energy balance given by the equations (58).

prohibitive for numerical purposes. In this subsection, we shown some strategies for the solution of this problems.

We first consider a small modification in the equilibrium distributions given by (51), (52) and (53) as follows. For $\mathbf{c}_1 = [0, 0, 0]$, let us introduce an extra coefficient α as

$$\begin{aligned}
 g_{1x}^{eq} &= (1 - w_1)B_x + \alpha B_x, \\
 g_{1y}^{eq} &= (1 - w_1)B_y + \alpha B_y, \\
 g_{1z}^{eq} &= (1 - w_1)B_z + \alpha B_z.
 \end{aligned} \tag{134}$$

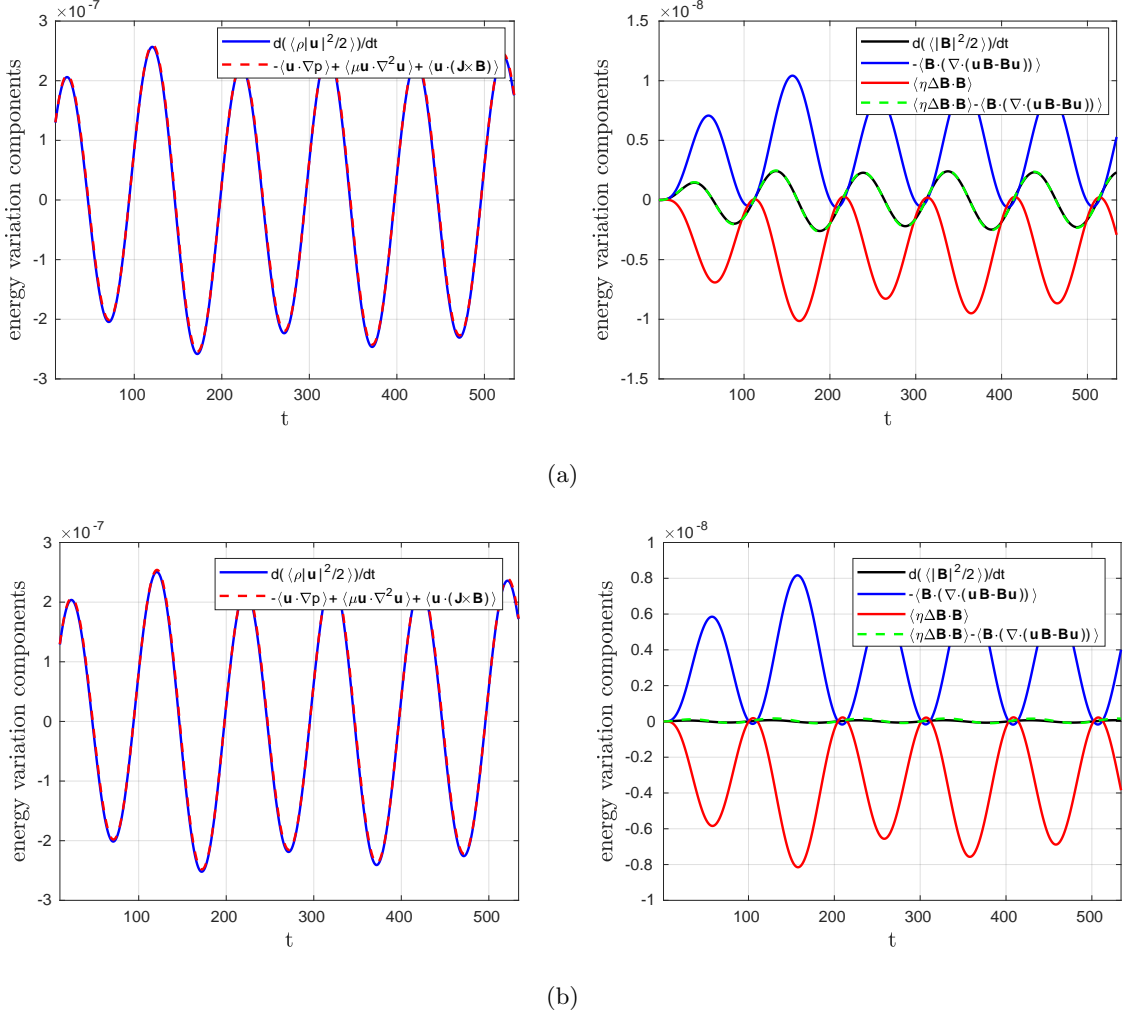


FIG. 8. In this figure we show the transition to the quasi-static regime. In (a) we show a simulation of a MHD flow in a circular pipe with radius $r = 22$, $Ha = 18$, $\eta = 2$ and $\nu = 0.08$ submitted to $\partial p / \partial x = -2.4 \times 10^{-4} \cos(2\pi t / 200)$ with $\lceil \frac{1}{\delta t} \rceil = N = 12$ iterations for (127). In (b), we set $\eta = 45$, which implies in $\lceil \frac{1}{\delta t} \rceil = N = 270$ iterations for the algorithm (127). We can observe in (b) the complete damping of the time derivative of the magnetic field, which is characteristic of the quasi-static approximation.

and for the other velocities $i = 2, \dots, N$, consider

$$\begin{aligned}
 g_{ix}^{eq} &= w_i \left[B_x + \frac{c_{iy}}{c_s^2} (u_y B_x - u_x B_y) + \frac{c_{iz}}{c_s^2} (u_z B_x - u_x B_z) \right], \\
 g_{iy}^{eq} &= w_i \left[B_y + \frac{c_{ix}}{c_s^2} (u_x B_y - u_y B_x) + \frac{c_{iz}}{c_s^2} (u_z B_y - u_y B_z) \right], \\
 g_{iz}^{eq} &= w_i \left[B_z + \frac{c_{ix}}{c_s^2} (u_x B_z - u_z B_x) + \frac{c_{iy}}{c_s^2} (u_y B_z - u_z B_y) \right],
 \end{aligned} \tag{135}$$

with the following small modification in the algorithm (127) given by

$$\begin{aligned} B_x(\mathbf{x}, t) &= \frac{1}{\alpha} \sum_{\alpha=1}^9 g_{x\alpha}^{eq}(\mathbf{x} - \mathbf{c}_\alpha \delta t, t - \delta t), \\ B_y(\mathbf{x}, t) &= \frac{1}{\alpha} \sum_{\alpha=1}^9 g_{y\alpha}^{eq}(\mathbf{x} - \mathbf{c}_\alpha \delta t, t - \delta t), \\ B_z(\mathbf{x}, t) &= \frac{1}{\alpha} \sum_{\alpha=1}^9 g_{z\alpha}^{eq}(\mathbf{x} - \mathbf{c}_\alpha \delta t, t - \delta t). \end{aligned} \quad (136)$$

By using the Chapman-Enskog multiscale expansion, it is possible to show that the algorithm (136) solves the following equation

$$\alpha \frac{\partial \mathbf{B}}{\partial t} + \nabla \cdot (\mathbf{u} \mathbf{B} - \mathbf{B} \mathbf{u}) = \eta \nabla^2 \mathbf{B}, \quad (137)$$

with a sufficient number of iterations. This procedure increases the convergence rate by a factor of $1/\alpha$, as we can see in the Figure 9. In this figure, a simulation with a variable pressure gradient given by the formula (59) is shown. In Figure 9(a), we show a simulation with the algorithm given by (136), where the algorithm for magnetic field is iterated $N = 9$ times before every iteration of the algorithm (54) for the momentum equation. The same experiment is performed by using the algorithm (127) with the same number of iterations, i.e., $N = 9$, recall that for the algorithm (127) the number of iterations is given by (130), which gives $N = 18$ for $\eta = 3$. We can see that the algorithm (136) converges to the (3) twice as fast in comparison with (127).

Values of α smaller than 0.5 can cause instabilities in (136), which limits the application of this procedure with respect to the quasi-static approximation. In Figure (8)(b), we see that the value of resistivity $\eta = 45$ is enough to make the time derivative $\frac{\partial \mathbf{B}}{\partial t}$ negligible, and the formula (130) gives $N = 270$ as the number of iterations needed to make the difference $|\eta \nabla^2 \mathbf{B} - \nabla \cdot (\mathbf{u} \mathbf{B} - \mathbf{B} \mathbf{u})|$ to be the same order of the time derivative, thus also negligible. We argue that the same number of iterations is also enough for values of resistivity much bigger than $\eta = 45$. In Figure (10), we compare the simulations with $\eta = 45$ and $\eta = 1000$ with the same number of iterations $N = 270$. In Figure (10)(a), we can see essentially the same results observed in Figure (8)(b) in the analysis of the energy budgets.

In order to calculate more accurately the dependence of the errors with respect to the resistivity with a fixed the number of iterations, we consider the following expression for the residual

$$\left\| \eta \nabla^2 \mathbf{B} - \nabla \cdot (\mathbf{u} \mathbf{B} - \mathbf{B} \mathbf{u}) \right\|_{L^2(\Omega)}, \quad (138)$$

where the differential operators are calculated by using isotropic finite difference schemes [29]. The residual is normalized by the initial residual, i.e., the residual at the first iteration. In Figure 10,

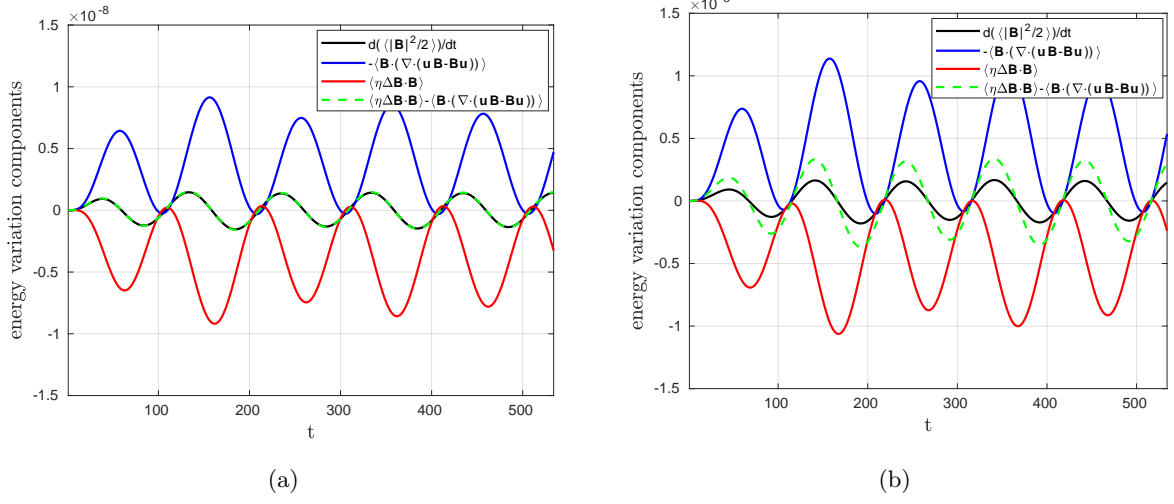


FIG. 9. Simulation with $\eta = 3$, $\nu = 0.08$, $Ha = 18$ and pipe radius $r = 22$. The variable pressure difference in this case is given by and $\frac{\partial p}{\partial x} = -1.9 \times 10^{-4} \cos(2\pi t/200)$. In picture (a), a simulation using the algorithm (136) is shown, where the convergence is reached with $N = 9$ iterations, which is half of the number of iterations recommend by the formula (130) for the algorithm (127), whose result with the same number of iterations is shown in picture (b).

we can see that the normalized error (138) does not change with the increase of the value of the resistivity, actually the value of the residual (138) is the same for $\eta = 45$ and $\eta = 1000$.

It suggests that for very high values of η we do not have to consider a too small value of δt (or very high number of iterations) given by the formula (130), instead we can actually consider an effective number of iterations defined by the number of iterations associated with the smallest value of resistivity that causes a satisfactory damping in the time derivative of the magnetic field, i.e., $|\frac{\partial \mathbf{B}}{\partial t}| \simeq 0$. An interesting feature of this procedure is that this convergence criterion avoids the need to calculate the residual (which is a non-local procedure) at each time step to guarantee convergence. An alternative procedure is given by solving the equation (132) using (127), which is equivalent to solve (133) in the QS regime. Both procedures produces the same results for the experiments of this article.

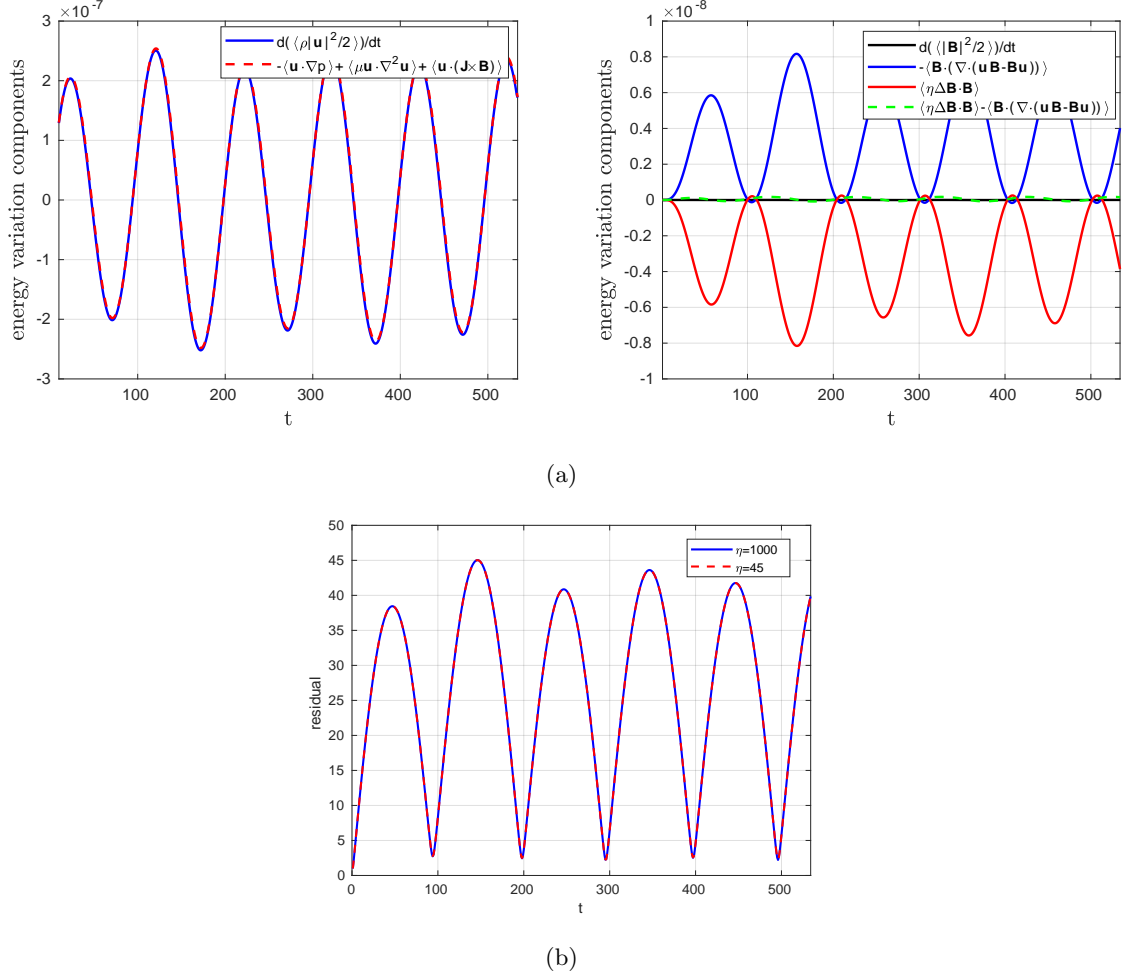


FIG. 10. Simulation of the quasi-static regime in a circular pipe with radius $r = 22$, $Ha = 18$ and $\nu = 0.08$ submitted to $\partial p / \partial x = -1.19 \times 10^{-4} \cos(2\pi t / 200)$. In the picture (a), the resistivity is set to $\eta = 1000$ with $N = 270$ iterations of the algorithm (127) for the magnetic field equations. The analysis of the residuals given by the expression (138) normalized by the initial residual is shown in picture (b), where we compare results for $\eta = 45$ and $\eta = 1000$.

VI. EFFECTS OF NON-UNIFORM MAGNETIC FIELDS

Most of the LBM simulations of MHD flows only considers the influence of uniform transversal magnetic fields. In this sections, we test the proposed algorithms developed in the previous sections

in problems involving an external non-uniform magnetic field, as for example, the field given by

$$\mathbf{B}_x(x, y, z) = 0, \quad (139)$$

$$\mathbf{B}_y(x, y, z) = 2 \left[\arctan \left(\frac{y-L}{z} \right) - \arctan \left(\frac{y+L}{z} \right) \right], \quad (140)$$

$$\mathbf{B}_z(x, y, z) = \log \left(\frac{(y+L)^2 + z^2}{(y-L)^2 + z^2} \right), \quad (141)$$

where (x, y, z) is a points in the fluid domain. These fields are obtained by using the Biot–Savart law [2], where L is the width of the slab’s rectangular cross section, which we assume to have aspect ratio 2. We consider $L = R/6$. The magnetic field lines generated by (140) and (141) in the yz -plane are shown in Figure 11(a); and in Figure 11(b) we shows the field lines of a combination of six magnets with alternating poles, where the magnetic field of each magnet can be mapped into the field given by (139), (140) and (141) by considering compositions with rotations and translations.

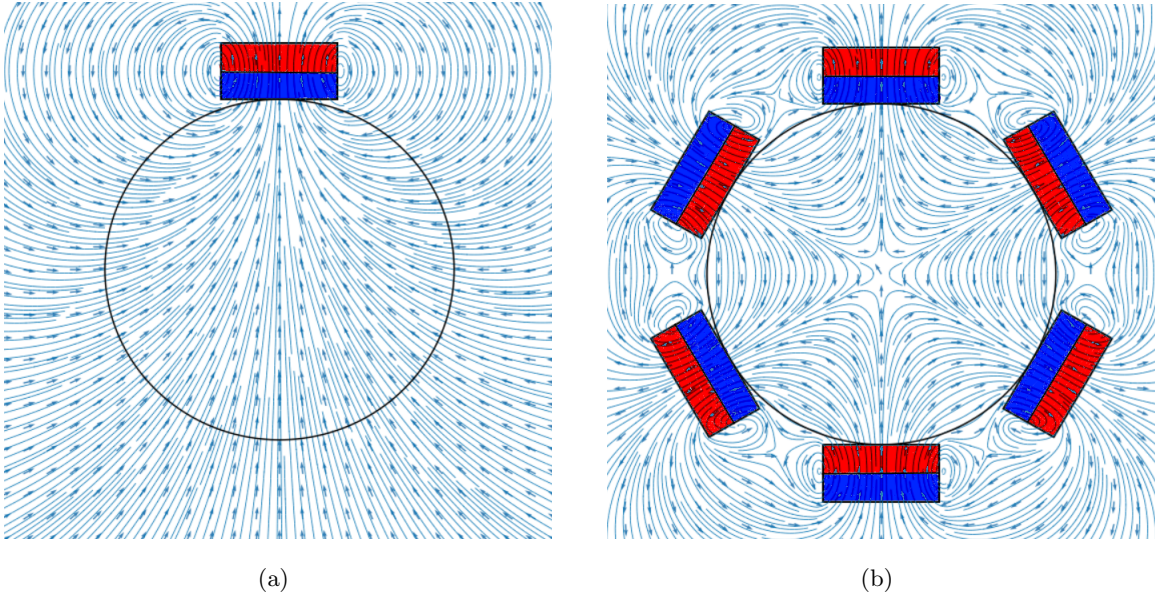


FIG. 11. (a) Magnetic field lines of one magnet generated by the field given by (140) and (141) in the yz -plane, where the red and blue colors indicate the north and south poles of the magnets, respectively. In (b), the magnetic field lines generated by a set of six magnets with alternating poles forming a hexagonal structure.

In Figure (12), we show a simulation of a MHD flow in a circular pipe based on the schematic representation shown in Figure 11(b), with viscosity $\nu = 0.04$, resistivity $\eta = 1000$, Hartman number $Ha = 20$ and pipe radius $r = 40$ in a computational grid with size $n_x \times n_y \times n_z = 5 \times 83 \times 83$. Periodic boundary conditions are considered in the streamwise direction and a constant body force $\frac{\partial p}{\partial x} = -2.16 \times 10^{-5}$ is imposed. In the Figures 12(a) and 12(b), we can observe the contour lines for

the velocity and magnetic fields showing the expected symmetry associated with the magnetic field configuration presented in Figure 11(b). The respective verification of the energy balance (58) is shown in Figure 12(c). The modification of the equilibrium distributions in order to implement the divergence of the Maxwell stress tensor [4], rather than the direct implementation of the Lorentz force, has not shown stable results for the cases involving non-uniform magnetic fields, indicating that for the algorithms presented in this article, the forcing term approach given by (69) is more suitable procedure.

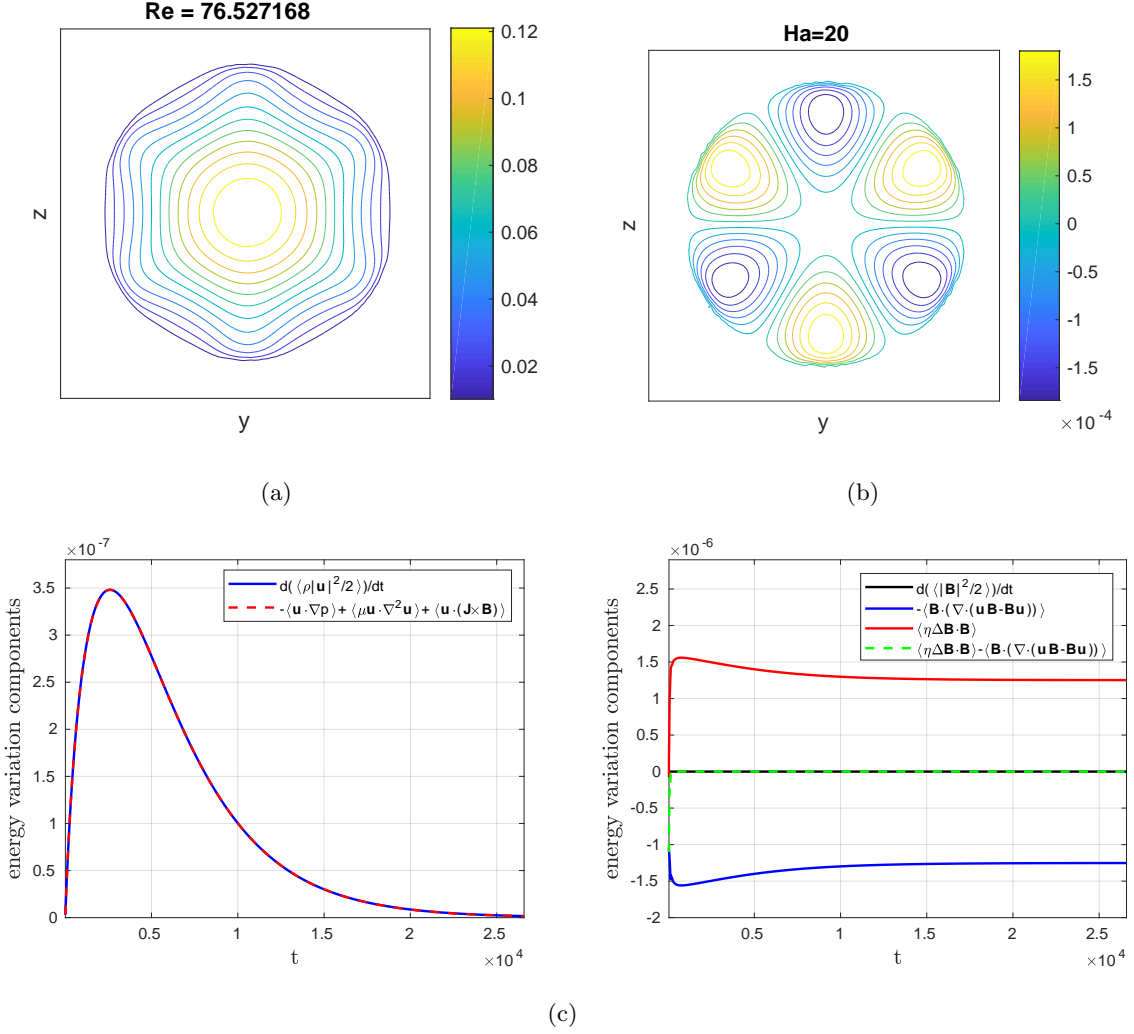


FIG. 12. Simulation of a MHD flows with the six magnets configuration in the quasi-static regime with $\eta = 1000$, $Ha = 20$, $\nu = 0.04$ and pipe radius $r = 38.5$. A constant body force with $\frac{\partial p}{\partial x} = -2.16 \times 10^{-5}$ is applied. The algorithm for the magnetic field (127) is iterated $N = 12$ times before every iteration of the algorithm for the velocity field (55). The simulation is performed until the stationary solution is obtained. In (a) and (b) we show some level curves for the velocity and magnetic fields, respectively. We can see that the velocity and magnetic field profiles verify the expected symmetries associated with the system (7-10). In (c) we show the verification of the energy balance equations given by (58).

VII. SIMULATIONS WITH MAGNETIC PRANDTL NUMBER $Pr_m > 1$

In all of the previous discussions, we concentrate our analysis in regimes with $Pr_m \leq 1$. In this section, we analyse the results of the single-step simplified algorithms proposed in this article for the case $Pr_m > 1$. This regime usually requires more accuracy of the numerical methods in space

and time. The few LBM results in the LBM literature [18, 19] about this regime are performed up to $Pr_m = 2$ by using more robust numerical schemes, such as the central-moments-based LBM in simulations with flat boundaries. In Figure 13(a), we can see a significant mismatch between numerical and analytical solution by using (55) with (127) in a simulation with $Pr_m = 4$, despite the improvements introduced in the previous sections.

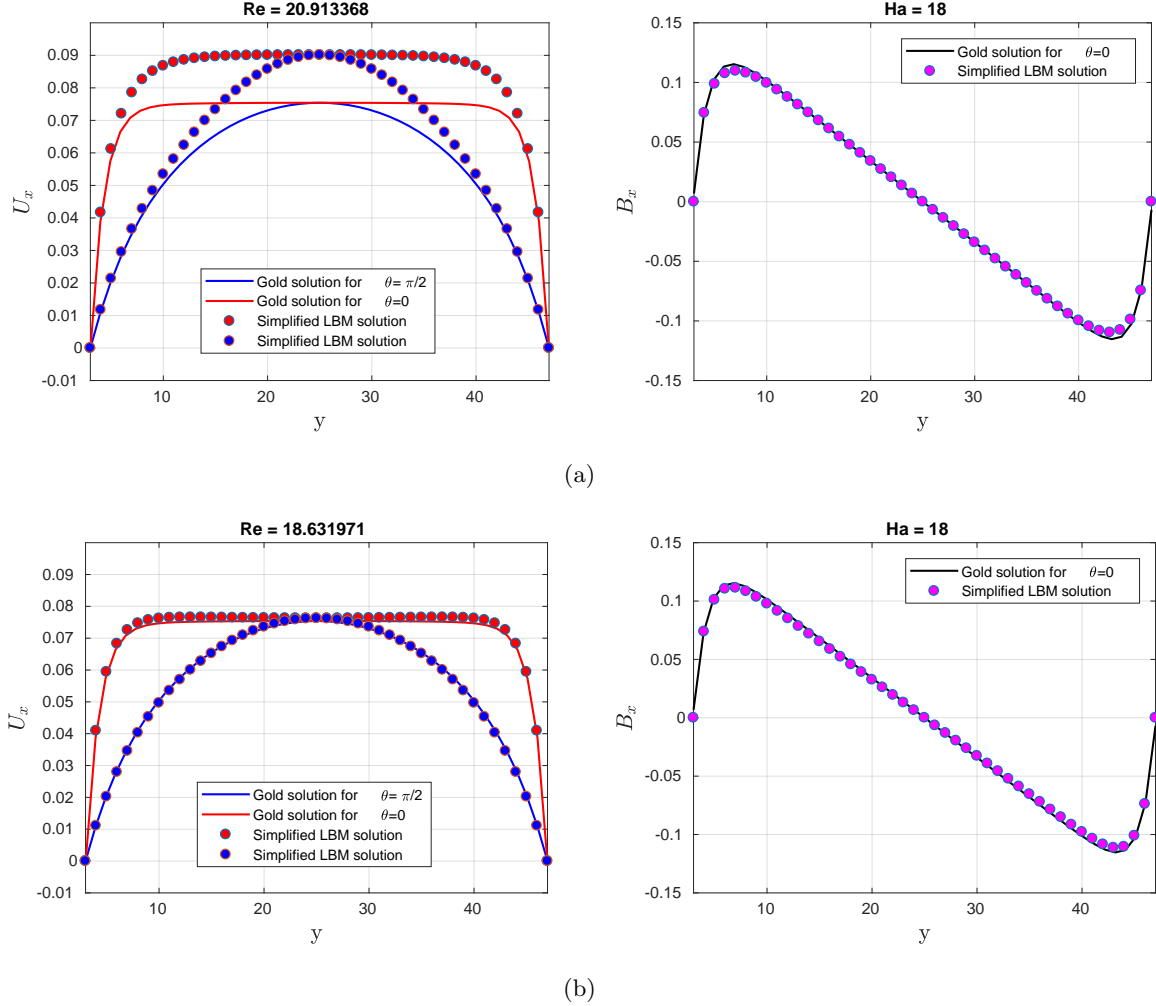


FIG. 13. MHD pipe flow simulations with $\nu = 0.08$, $\eta = 0.02$, $Ha = 18$ and pipe radius $r = 22$ with $\gamma = 1$ in picture (a), and $\gamma = 4$ in picture (b). A constant body force with $\frac{\partial p}{\partial x} = -2.38 \times 10^{-4}$ is applied. It is possible to observe a significant loss of spatial accuracy in (a), which is restored by using the rescaled simplified single-step LBM solution obtained by using (142) and (143), as we can see in picture (b).

In order to solve this problem we consider a strategy based in the introduction of a smaller time steps. Most of the simplified LBM methods are constructed considering $\delta t = \delta x$, which restricts the possibilities of the changes of δt to some particular grid configurations. In order to avoid this limitation, we consider a set of rescaled variables, indicated by overlines, associated with an extra

parameter γ verifying

$$\overline{\delta t} = \frac{\delta t}{\gamma}, \quad (142)$$

with rescaled lattice velocities $\overline{\mathbf{c}}_i$ and speed of sound \overline{c}_s verifying

$$\overline{\mathbf{c}}_i = \gamma \mathbf{c}_i \quad \text{and} \quad \overline{c}_s = \frac{\gamma c}{\sqrt{3}} = \gamma c_s, \quad (143)$$

which means that we are keeping the computational grid unchanged, i.e., $\delta x = \overline{\delta x}$. Assuming that the density is not affected by the transformations, i.e., $\overline{\rho} \simeq \rho$, it turns out that the substitution of scaling relationships (142) and (143) in the demonstration of the single-step algorithm (54) is equivalent to consider the original algorithm (where $\delta x = \delta t$) with the rescaled equilibrium distributions

$$f_i^{eq}(x, t) = w_i \rho \left[1 + \frac{\mathbf{c}_i \cdot \mathbf{u}}{c_s^2} + \frac{1}{\gamma} \left(\frac{(\mathbf{c}_i \cdot \mathbf{u})^2}{2c_s^4} - \frac{\mathbf{u} \cdot \mathbf{u}}{2c_s^2} \right) \right], \quad (144)$$

$$g_{ix}^{eq}(x, t) = w_i \left[B_x + \frac{1}{\gamma} \left(\frac{c_{iy}}{c_s^2} (u_y B_x - u_x B_y) + \frac{c_{iz}}{c_s^2} (u_z B_x - u_x B_z) \right) \right], \quad (145)$$

$$g_{iy}^{eq}(x, t) = w_i \left[B_y + \frac{1}{\gamma} \left(\frac{c_{ix}}{c_s^2} (u_x B_y - u_y B_x) + \frac{c_{iz}}{c_s^2} (u_z B_y - u_y B_z) \right) \right], \quad (146)$$

$$g_{iz}^{eq}(x, t) = w_i \left[B_z + \frac{1}{\gamma} \left(\frac{c_{ix}}{c_s^2} (u_x B_z - u_z B_x) + \frac{c_{iy}}{c_s^2} (u_y B_z - u_z B_y) \right) \right], \quad (147)$$

and rescaled relaxation times given by

$$\tau = \frac{\nu}{\overline{c}_s^2 \overline{\delta t}} + \frac{1}{2} = \frac{\nu}{\gamma c_s^2 \delta t} + \frac{1}{2}, \quad (148)$$

and

$$\tau_m = \frac{\eta}{\overline{c}_s^2 \overline{\delta t}} + \frac{1}{2} = \frac{\eta}{\gamma c_s^2 \delta t} + \frac{1}{2}, \quad (149)$$

which are defined in such a way to keep the viscosities and resistivities unchanged by the transformations (142) and (143). If we consider the inclusion of the FGS forcing term (61) in the simplified algorithm, then the introduction of (143) also leads to

$$F_i = \left(1 - \frac{1}{2\tau} \right) w_i \left[\frac{(\mathbf{c}_i - \frac{\mathbf{u}}{\gamma})}{\gamma c_s^2} + \frac{(\mathbf{c}_i \cdot \mathbf{u})}{\gamma^2 c_s^4} \mathbf{c}_i \right] \cdot \mathbf{F}_{ext}. \quad (150)$$

with τ given by (148). All of these modifications provide essentially the same result as those obtained using the preconditioning procedures described in [7, 15–17]. The same equations can also be found by using the strategy of the adaptive time step (ATS) developed in [35], with the exception of the treatment of the nonequilibrium terms.

If we consider we consider $\gamma > 1$, we essentially decrease of the effective time step by a factor of $1/\gamma$. Consequently, we obtain a significant improvement of the accuracy with minimum changes in the original single-step algorithm. Naturally, γ cannot be changed arbitrarily, if γ is too small, some transient phenomena with typical small time scales may be missed, and if γ is too large, simulations may have an excessively slow convergence rate with some possible loss of accuracy, due to the fact that the scalings can make the relaxation times to close to the value 0.5 if $\gamma \gg 1$.

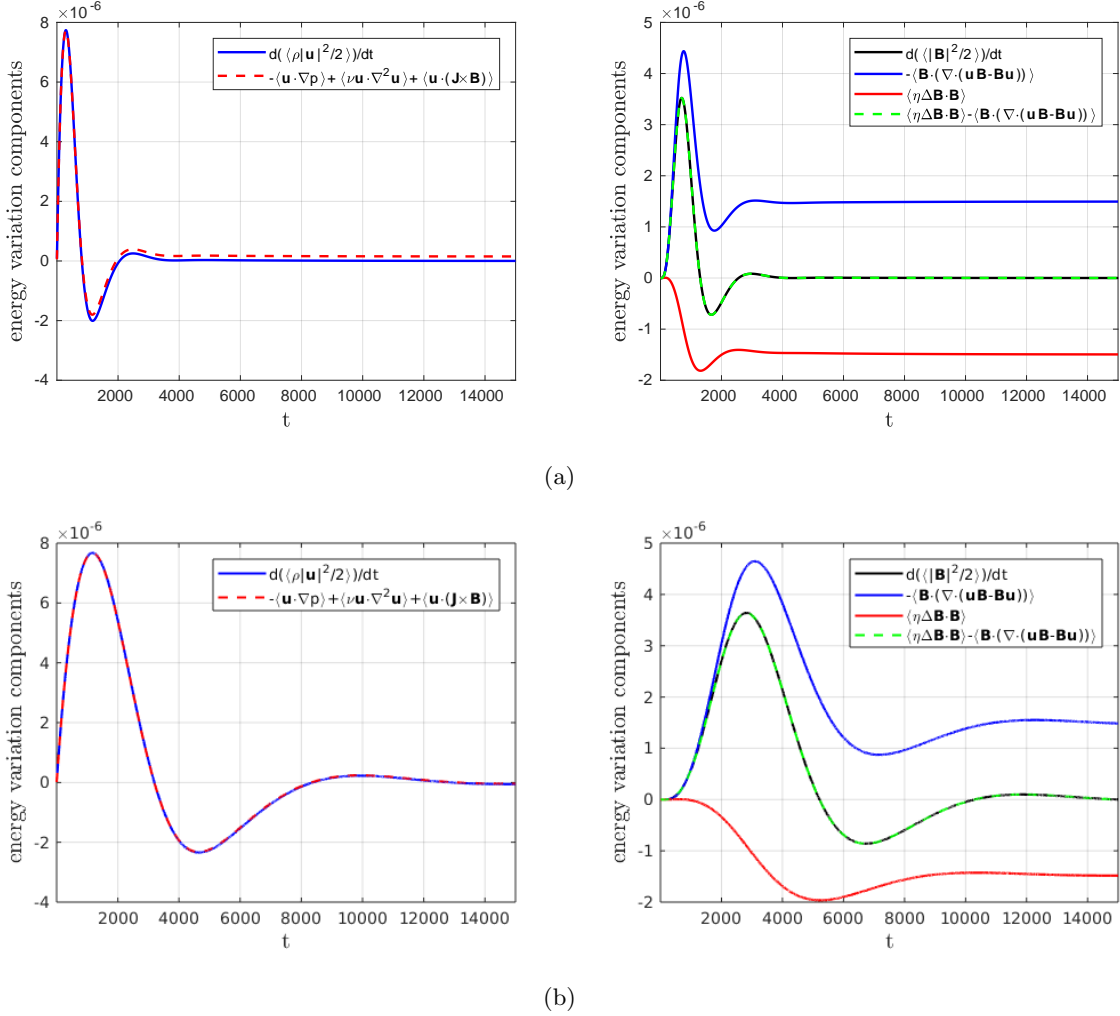


FIG. 14. MHD pipe flow simulation with $\nu = 0.08$, $\eta = 0.02$, $Ha = 18$ and pipe radius $r = 22$. A constant body force with $\frac{\partial p}{\partial x} = -2.38 \times 10^{-4}$ is applied. In picture (a), we show results of the analysis of the energy balance (58) for $\gamma = 1$, and in picture (b), the results for $\gamma = 4$. By analysing the transient part in the energy budgets, we can observe an increase of the accuracy in time by using the rescaled simplified single-step LBM solution obtained by introducing (142) and (143).

In the Figures 13 and 14, we performed some MHD pipe flow simulations with $\nu = 0.08$, $\eta = 0.02$, $Ha = 18$ and pipe radius $r = 22$. A constant body force with $\frac{\partial p}{\partial x} = -2.38 \times 10^{-4}$ is

applied. The computational grid size considered is $n_x \times n_y \times n_z = 5 \times 50 \times 50$. In Figures 13(b) and 14(b), we show the velocity and magnetic field statistics associated with the scaling $\gamma = 4$; and in Figures 13(a) and 14(a), we present the statistics generated by using $\gamma = 1$. In the Figure 14, it is possible to see that the solutions were essentially rescaled in time by a factor of γ . Not only that, we can also observe a significant improvement of the accuracy in space (verification of the Gold's solutions) and time (correct verification of the energy balance).

VIII. CONCLUSIONS

In this article, we provide a set of extensions and improvements in a class of simplified LBM algorithms with the objective to simulate MHD flows with very small magnetic Reynolds numbers in pipe flows. We also introduce a immersed boundary method able to accurately include the effects curved insulating walls in the MHD equations and whose accuracy is not significantly dependent on the values of the relaxation times. Improvements in the implementation of forcing term allows an accurate and stable implementation of variable forcing terms, showing good results even in the presence of strongly non-uniform magnetic fields. With this set of improvements, in the present work we provide a completely local and explicit LBM framework for simulations of the quasi-static approximation in pipe flows, with a good potential for simulations involving more complex geometries.

By considering an adaptive time step strategy, we were able to increase the precision of the single-step LBM algorithm in space and time with minimal changes in the general form of the algorithm, extending the applicability of the method to some regimes up to $Pr_m = 4$, which have not yet been analyzed in the LBM literature. It is also important to mention that results introduced in this article can be extend as well to some other simplified lattice Boltzmann models [14, 21, 22, 34].

As future works and suggestions, further verification of the proposed methods for turbulent flows and extensions for the cases involving conducting curved walls are natural future directions for this research, as well as systematic comparisons with similar solutions provided by other numerical methods. Also, the use of of more robust LBM schemes such as MRT (multiple-relaxation-time) and central-moments-based schemes for the magnetic field equations can be interesting options towards the same objectives of this article, with some possible improvements in terms of accuracy [36].

ACKNOWLEDGEMENTS

The authors acknowledge the support given to this work by the project entitled “Experimental study of inorganic fouling in sand containment systems”, established by agreement between the COPPETEC Foundation (COPPE/UFRJ) and the oil company Petróleo Brasileiro S.A. (Petrobras), with the project of number 21.389. They also thank the Interdisciplinary Center of Fluid Dynamics (NIDF) at UFRJ, which was of great help in terms of people, infrastructure and resources for the research presented in this article.

-
- [1] P. A. Davidson, An introduction to magnetohydrodynamics (2002).
 - [2] B. Knaepen, S. Kassinos, D. Carati, Magnetohydrodynamic turbulence at moderate magnetic reynolds number, *Journal of Fluid Mechanics* 513 (2004) 199–220.
 - [3] U. Müller, L. Bühler, Magnetofluidynamics in channels and containers, Springer Science & Business Media, 2001.
 - [4] A. De Rosis, R. Liu, A. Revell, One-stage simplified lattice boltzmann method for two-and three-dimensional magnetohydrodynamic flows, *Physics of Fluids* 33 (8) (2021) 085114.
 - [5] M. Pattison, K. Premnath, N. Morley, M. Abdou, Progress in lattice boltzmann methods for magnetohydrodynamic flows relevant to fusion applications, *Fusion Engineering and Design* 83 (4) (2008) 557–572.
 - [6] A. De Rosis, R. Huang, C. Coreixas, Universal formulation of central-moments-based lattice boltzmann method with external forcing for the simulation of multiphysics phenomena, *Physics of Fluids* 31 (11) (2019) 117102.
 - [7] K. N. Premnath, M. J. Pattison, S. Banerjee, Steady state convergence acceleration of the generalized lattice boltzmann equation with forcing term through preconditioning, *Journal of Computational Physics* 228 (3) (2009) 746–769.
 - [8] A. Delgado-Gutiérrez, P. Marzocca, D. Cárdenas, O. Probst, A single-step and simplified graphics processing unit lattice boltzmann method for high turbulent flows, *International Journal for Numerical Methods in Fluids* 93 (7) (2021) 2339–2361.
 - [9] Y. Gao, L. Yang, Y. Yu, G. Hou, Z. Hou, Consistent forcing scheme in the simplified lattice boltzmann method for incompressible flows, *Communications in Computational Physics* 30 (5) (2021) 1427–1452.
 - [10] Z. Chen, C. Shu, D. Tan, X. Niu, Q. Li, Simplified multiphase lattice boltzmann method for simulating multiphase flows with large density ratios and complex interfaces, *Physical Review E* 98 (6) (2018) 063314.
 - [11] T. Krüger, H. Kusumaatmaja, A. Kuzmin, O. Shardt, G. Silva, E. M. Viggien, The lattice Boltzmann method, Springer International Publishing 10 (2017) 978–3.

- [12] S. Succi, The lattice Boltzmann equation: for complex states of flowing matter, Oxford University Press, 2018.
- [13] S. Gsell, U. d’Ortona, J. Favier, Explicit and viscosity-independent immersed-boundary scheme for the lattice boltzmann method, *Physical Review E* 100 (3) (2019) 033306.
- [14] J. G. Zhou, Macroscopic lattice boltzmann method, *Water* 13 (1) (2020) 61.
- [15] Z. Guo, T. Zhao, Y. Shi, Preconditioned lattice-boltzmann method for steady flows, *Physical Review E* 70 (6) (2004) 066706.
- [16] S. Izquierdo, N. Fueyo, Preconditioned navier-stokes schemes from the generalised lattice boltzmann equation, *Progress in Computational Fluid Dynamics, an International Journal* 8 (1-4) (2008) 189–196.
- [17] E. Turkel, Preconditioning techniques in computational fluid dynamics, *Annual Review of Fluid Mechanics* 31 (1) (1999) 385–416.
- [18] A. De Rosis, E. L  v  que, R. Chahine, Advanced lattice boltzmann scheme for high-reynolds-number magneto-hydrodynamic flows, *Journal of Turbulence* 19 (6) (2018) 446–462.
- [19] A. De Rosis, A. Skillen, Vortex dynamics in an electrically conductive fluid during a dipole–wall collision in presence of a magnetic field, *Physics of Fluids* 34 (8) (2022) 081704.
- [20] D. A. Wolf-Gladrow, *Lattice-gas cellular automata and lattice Boltzmann models: an introduction*, Springer, 2004.
- [21] Z. Chen, C. Shu, Y. Wang, L. Yang, D. Tan, A simplified lattice boltzmann method without evolution of distribution function, *Advances in Applied Mathematics and Mechanics* 9 (1) (2017) 1–22.
- [22] C. Shu, Y. Wang, C. Teo, J. Wu, Development of lattice boltzmann flux solver for simulation of incompressible flows, *Advances in Applied Mathematics and Mechanics* 6 (4) (2014) 436–460.
- [23] S. Chen, G. D. Doolen, Lattice boltzmann method for fluid flows, *Annual review of fluid mechanics* 30 (1) (1998) 329–364.
- [24] U. Frisch, *Turbulence: the legacy of A. N. Kolmogorov*, Cambridge university press, 1995.
- [25] P. J. Dellar, Lattice kinetic schemes for magnetohydrodynamics, *Journal of Computational Physics* 179 (1) (2002) 95–126.
- [26] X. Zhao, Z. Chen, L. Yang, N. Liu, C. Shu, Efficient boundary condition-enforced immersed boundary method for incompressible flows with moving boundaries, *Journal of Computational Physics* 441 (2021) 110425.
- [27] R. R. Gold, Magneto-hydrodynamic pipe flow. part 1, *Journal of Fluid Mechanics* 13 (4) (1962) 505–512.
- [28] Z. Guo, C. Zheng, B. Shi, Discrete lattice effects on the forcing term in the lattice boltzmann method, *Physical review E* 65 (4) (2002) 046308.
- [29] S. P. Thampi, S. Ansumali, R. Adhikari, S. Succi, Isotropic discrete laplacian operators from lattice hydrodynamics, *Journal of Computational Physics* 234 (2013) 1–7.
- [30] F. A. Amiri, G. Le, Q. Chen, J. Zhang, Accuracy improvement for immersed boundary method using lagrangian velocity interpolation, *Journal of Computational Physics* 423 (2020) 109800.
- [31] G. H. Golub, C. F. Van Loan, *Matrix computations*, JHU press, 2013.

- [32] J.-J. Climent, N. Thome, Y. Wei, A geometrical approach on generalized inverses by neumann-type series, *Linear algebra and its applications* 332 (2001) 533–540.
- [33] K. Tanabe, Neumann-type expansion of reflexive generalized inverses of a matrix and the hyperpower iterative method, *Linear Algebra and Its Applications* 10 (2) (1975) 163–175.
- [34] T. Inamuro, A lattice kinetic scheme for incompressible viscous flows with heat transfer, *Philosophical Transactions of the Royal Society of London. Series A: Mathematical, Physical and Engineering Sciences* 360 (1792) (2002) 477–484.
- [35] T. Horstmann, H. Touil, L. Vienne, D. Ricot, E. Lévêque, Consistent time-step optimization in the lattice boltzmann method, *Journal of Computational Physics* 462 (2022) 111224.
- [36] B. Magacho, H. S. Tavares, L. Moriconi, J. Loureiro, Double multiple-relaxation-time model of lattice-boltzmann magnetohydrodynamics at low magnetic reynolds numbers, *arXiv preprint arXiv:2211.11005* (2022).